

Low-energy collective electronic excitations in LiC_6 , SrC_6 , and BaC_6

J. P. Echeverry,¹ E. V. Chulkov,^{2,3,4} P. M. Echenique,^{2,3,4} and V. M. Silkin^{2,3,5}

¹Universidad de Ibagué, Cra. 22 Calle 67 Barrio Ambalá, CP 730010 Ibagué-Tolima, Colombia

²Donostia International Physics Center (DIPC), Paseo de Manuel Lardizabal 4, E-20018 San Sebastián, Basque Country, Spain

³Departamento de Física de Materiales, Facultad de Ciencias Químicas, Universidad del País Vasco (UPV-EHU),
Apdo. 1072, E-20080 San Sebastián, Basque Country, Spain

⁴Centro de Física de Materiales (CFM), Materials Physics Center (MPC), Centro Mixto CSIC–UPV/EHU,
Paseo de Manuel Lardizabal 5, E-20018 San Sebastián, Basque Country, Spain

⁵IKERBASQUE, Basque Foundation for Science, E-48011 Bilbao, Basque Country, Spain



(Received 25 May 2019; revised manuscript received 3 September 2019; published 17 September 2019)

We present a first-principles study of the electronic band structure and low-energy dielectric response properties of a representative group of graphite intercalated compounds— LiC_6 , SrC_6 , and BaC_6 . Our results obtained from time-dependent density functional theory calculations reveal the presence of different plasmons in these compounds at energies below 12 eV. The presence of these collective electronic excitations is discussed in terms of intra- and interband transitions. In addition to the bulk plasmon, we find the π - and intraband plasmons. However, their properties vary greatly from one material to another. In LiC_6 and BaC_6 , the π plasmon is a two-dimensional excitation, whereas in SrC_6 it has a three-dimensional character. As for the intraband plasmon, it is observed in all momentum-transfer symmetry directions, with rather strong anisotropy in the energy position between momentum transfers in the basal carbon plane and perpendicular to it. Also, we discuss the appearance in SrC_6 and BaC_6 of a low-energy collective electronic mode with the characteristic soundlike dispersion in terms of the energy bands crossing the Fermi level with different group velocities. We find a correlation between the appearance of such low-energy electronic modes and the occupation of the graphite interlayer band.

DOI: [10.1103/PhysRevB.100.115137](https://doi.org/10.1103/PhysRevB.100.115137)

I. INTRODUCTION

Graphite intercalated compounds (GICs) consist of stacked carbon layers hosting dopants between them (atoms or molecules) that modify dramatically the physical properties of the host [1]. After intercalation with some metals, graphite becomes superconducting with a critical temperature (T_c) varying in a wide range (1–11 K) depending on the dopant [2–6]. This fact has renewed the interest in electronic properties of GICs [7–16] and, in particular, in the changes of the graphite's electronic properties produced by the intercalation process.

While it is generally accepted that superconductivity in GICs is driven by the Bardeen-Cooper-Schrieffer (BCS) mechanism with conventional electron-phonon coupling [17,18], there are still some inconsistencies between the data obtained from measurements of the isotope effect [19] and specific heat [20–22], as was pointed out some time ago [23]. Likewise, the relevance of the carbon or intercalant phonon modes in the overall electron-phonon coupling has been actively investigated [10,13,24–27].

In the intercalation process, the GIC's number of electronic states at the Fermi level can vary strongly in contrast to the pure graphite, where the concentration of electrons and holes at the Fermi level is small. Considerable effort has been devoted to understanding the modifications in the electronic band structure over the intercalation process, such as the alteration of the carbon-derived energy bands and the charge-transfer processes from the foreign atoms to carbon layers

[28–30]. In this respect, special attention was given to the study of the evolution of a so-called interlayer energy band, which is totally unoccupied in pristine graphite and becomes partially occupied in some GICs [31].

In fact, soon after the discovery of enhanced T_c in YbC_6 ($T_c = 6.5$ K) and CaC_6 ($T_c = 11.5$ K), an interesting observation was made by Csányi *et al.* concerning the electronic structure of several superconducting and nonsuperconducting GICs [31]. They noted a correlation between the occupation of the interlayer energy band and superconductivity, suggesting that the interlayer band plays a crucial role in the superconductivity phenomenon in these compounds. Based on this analysis, it was speculated that an electronic mechanism might be at the origin of superconductivity in those GICs where the interlayer band is partly occupied. In particular, it was suggested that since at the Fermi level there are two kinds of carriers in the energy bands (the carbon-derived π^* band and the interlayer band), a so-called acoustic plasmon (AP) could exist and play the role of a mediator, like phonons in the BCS scenario [32–35].

An important theoretical prediction in a metal-atom-covered graphene system based on bulk properties of GICs was made by Profeta *et al.* [8]. They predicted that LiC_6 , a nonsuperconductor compound in bulk form, becomes a superconductor with $T_c = 8.1$ K in its thinnest limit consisting of a layer of Li on top of graphene. Later on, by using angle-resolved high-resolution spectroscopy, Ludbrook *et al.* demonstrated that the Li-decorated monolayer graphene is indeed superconducting with $T_c = 5.9$ K [36]. Recently,

Ichinokura *et al.* [37] studied bilayers of graphene intercalated by calcium and lithium, C_6CaC_6 and C_6LiC_6 . They used electrical transport measurements to demonstrate that the Ca-intercalated graphene bilayer exhibits a superconducting phase like that of its bulk counterpart, while C_6LiC_6 is concluded to be a nonsuperconductor in line with bulk LiC_6 but differing from the Li-decorated graphene [38]. Since in the LiC_6 bulk band structure the interlayer band is unoccupied and in the Li-decorated graphene it becomes semioccupied, the doping via metal adatom intercalation seems to be the major factor in the superconducting mechanism of GICs.

Recently, the AP was predicted to exist in CaC_6 , where the interlayer band is partly occupied. The appearance of this peculiar three-dimensional (3D) low-energy plasmon with a soundlike dispersion is due to the presence of carriers with different Fermi velocities at the Fermi level [39]. Those carriers correspond to three kinds of energy bands crossing the Fermi level, namely interlayer, carbon-derived, and hybridized bands (carbon-derived bands whose dispersion is strongly modified upon intercalation).

By using high-resolution electron energy-loss spectroscopy (EELS) in transmission geometry, Roth *et al.* studied the low-energy collective electronic excitations in CaC_6 [40]. Their results on the dispersion and energy in the optical limit of the π -plasmon as well as the intraband plasmon (IP) are in reasonable agreement with theoretical results [39]. However, a finite value of 1.0 eV in the optical limit was measured for the low-energy mode [40]. This result contrasts with the theoretical findings predicting that the AP energy goes to zero as the momentum transfer approaches the optical limit. We are aware that despite the experimental observation of a mode with similar soundlike dispersion [41] at metal surfaces [42–45], the detection of this kind of electronic excitation in the bulk is experimentally challenging. In this case, we believe that theory can provide valuable results to shed light on complex problems such as this and find new candidates for experimental detection.

In this work, we present a first-principles study of the electronic structure and dielectric response properties of a representative set of GICs. The calculations in the framework of the time-dependent density functional theory (TDDFT) were performed with full inclusion of the *ab initio* energy band structure evaluated in a self-consistent pseudopotential scheme. In particular, we analyze the role of the occupation of the interlayer band in the appearance of the low-energy electronic modes for systems in which graphite hosts different intercalants providing distinct electron concentration. For this reason, three GICs were chosen to be considered. In LiC_6 , a nonsuperconductor GIC, the interlayer band is totally empty, while in the superconducting BaC_6 and SrC_6 [5,6], the interlayer band is partly occupied.

The rest of the paper is organized as follows. In Sec. II, a brief description of the methods used and some computational details are given. In Sec. III, we present the electronic structure of the materials under study, the calculated dielectric function, and the energy-loss spectra along certain symmetry directions. A summary and conclusions are presented in Sec. IV. Unless otherwise stated, atomic units ($\hbar = e^2 = m_e = 1$) are used throughout the paper.

TABLE I. Crystal structure parameters, stacking sequence, symmetry group, and carbon interlayer distance d of a representative set of GICs. Here a and c are the lattice parameters of the hexagonal structures [22,39,46].

System	a (Å)	c (Å)	Stacking sequence	Sym. group	d (Å)
LiC_6	4.28	3.70	$A\alpha$	P_6/mmm	3.70
CaC_6	4.33	13.57	$A\alpha A\beta A\gamma$	$R\bar{3}m$	4.52
SrC_6	4.32	9.90	$A\alpha A\beta$	$P6_3/mmc$	4.95
BaC_6	4.26	10.50	$A\alpha A\beta$	$P6_3/mmc$	5.25
YbC_6	4.32	9.15	$A\alpha A\beta$	$P6_3/mmc$	4.58

II. CALCULATION METHODS AND DETAILS

The crystal structure parameters of the materials under study are listed in Table I. Also, for the sake of comparison, we report there the parameters for other representative GIC's, namely CaC_6 and YbC_6 . Additionally, Table I contains symmetry groups, a stacking sequence, and carbon interlayer distances in these systems. In general, the atomic lattice in GIC's can form one of the $A\alpha$, $A\alpha A\beta$, or $A\alpha A\beta A\gamma$ stacking sequences, where graphite layers denoted by A have the same arrangement, while the intercalant (Li, Ca, Sr, Ba, or Yb) atoms occupy interlayer sites above the centers of the carbon hexagons in one of the three possible α , β , or γ positions (see Fig. 1).

The hexagonal unit cell of LiC_6 contains one Li and six C atoms, while in SrC_6 (BaC_6) it contains two Sr (Ba) and twelve C atoms. A general unit cell of a GIC from the lateral and the top view and the corresponding first Brillouin zone (1BZ) of the hexagonal unit cell are shown in Fig. 1. A definition of the main symmetry directions in the crystal and in the reciprocal space is given there as well.

We calculated the band structure of LiC_6 , SrC_6 , and BaC_6 within the self-consistent density functional theory employing a homemade band-structure code [47]. The valence-core interaction was described by Troullier-Martin norm-conserving

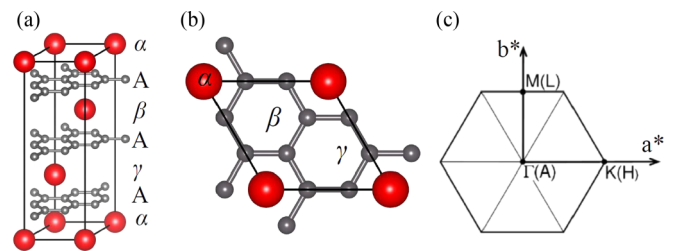


FIG. 1. (a),(b) Hexagonal unit cell and stacking sequence of GICs. All carbon atomic layers denoted by A have the same arrangement in the basal plane as shown by small gray circles. Large red circles represent intercalant atoms located in the interlayer positions above the centers of carbon hexagons in α or β or γ site as schematized in (b). (c) Projection of the first Brillouin zone (1BZ) onto the hexagonal carbon basal plane. In (c) the ΓKM and AHL planes cross the c^* axis, directed in the direction perpendicular to the basal plane, at $k_z = 0$ and $k_z = \pi/c$, respectively. In the reciprocal space, three main symmetry directions of the momentum transfer— a^* , b^* , and c^* —are directed along the ΓK , ΓM , and ΓA directions of the 1BZ, respectively.

pseudopotentials [48]. The self-consistent Kohn-Sham eigenvalues $\varepsilon_{n\mathbf{k}}$ and eigenfunctions $\psi_{n\mathbf{k}}(\mathbf{r})$ were obtained with the use of the exchange-correlation potential in the form of Ref. [49]. In a self-consistent procedure, the summation over wave vectors in the irreducible part of the 1BZ was performed over a $16 \times 16 \times 12$ \mathbf{k} mesh in the case of LiC_6 . In the case of SrC_6 and BaC_6 , the $16 \times 16 \times 6$ \mathbf{k} mesh was used. For the expansion of the wave functions, a plane-wave basis set with an energy cutoff of 50 Ry was employed.

The macroscopic dielectric function ε_M probed in optical experiments is given by $\varepsilon_M(\mathbf{Q}, \omega) = 1/\varepsilon_{\mathbf{G}\mathbf{G}}^{-1}(\mathbf{q}, \omega)$, where ω and \mathbf{Q} are the energy and the momentum transfer, respectively. In general, $\mathbf{Q} = \mathbf{q} + \mathbf{G}$, where the vector \mathbf{q} belongs to the 1BZ and \mathbf{G} 's are the reciprocal-lattice vectors. The energy-loss function, $L(\mathbf{Q}, \omega) \equiv -\text{Im}[\varepsilon_{\mathbf{G}\mathbf{G}}^{-1}(\mathbf{q}, \omega)]$, is proportional to the dynamical structure factor $S(\mathbf{Q}, \omega) \sim -\text{Im}[\varepsilon_{\mathbf{G}\mathbf{G}}^{-1}(\mathbf{q}, \omega)]$ directly probed in the inelastic x -ray scattering and electron-energy-loss experiments. The inverse dielectric function ε^{-1} can be written in terms of the density-response function of interacting electrons, χ , in the form

$$\varepsilon_{\mathbf{G}\mathbf{G}'}^{-1}(\mathbf{q}, \omega) = \delta_{\mathbf{G}\mathbf{G}'} + V_{\mathbf{G}}(\mathbf{q})\chi_{\mathbf{G}\mathbf{G}'}(\mathbf{q}, \omega), \quad (1)$$

where $V_{\mathbf{G}}(\mathbf{q})$ is the Fourier transform of the bare Coulomb potential V .

$$\chi_{\mathbf{G}\mathbf{G}'}^0(\mathbf{q}, \omega) = \frac{2}{\Omega} \sum_{\mathbf{k}} \sum_{n, n'} \frac{(f_{n\mathbf{k}} - f_{n'\mathbf{k}+\mathbf{q}}) \langle \psi_{n\mathbf{k}} | e^{-i(\mathbf{q}+\mathbf{G})\cdot\mathbf{r}} | \psi_{n'\mathbf{k}+\mathbf{q}} \rangle \langle \psi_{n'\mathbf{k}+\mathbf{q}} | e^{i(\mathbf{q}+\mathbf{G}')\cdot\mathbf{r}} | \psi_{n\mathbf{k}} \rangle}{\varepsilon_{n\mathbf{k}} - \varepsilon_{n'\mathbf{k}+\mathbf{q}} + (\omega + i\eta)}. \quad (3)$$

Here the factor 2 accounts for spin, Ω is the normalization volume, $f_{n\mathbf{k}}$ is the Fermi distribution function, and η is a positive infinitesimal. The evaluation of the Fourier coefficients $\chi_{\mathbf{G}\mathbf{G}'}^0(\mathbf{q}, \omega)$ was realized using our homemade code designed for the dielectric function calculations [54]. It is the most time-consuming part of the current calculations. To reduce the computation cost, we follow the approach described in Refs. [55–57]. It consists in the evaluation of the imaginary part of the $\chi_{\mathbf{G}\mathbf{G}'}^0(\mathbf{q}, \omega)$ matrix elements according to

$$\begin{aligned} \chi_{\mathbf{G}\mathbf{G}'}^{\text{ol}}(\mathbf{q}, \omega) &= \frac{2}{\Omega} \sum_{\mathbf{k}} \sum_n^{\text{occ}} \sum_{n'}^{\text{unocc}} \langle \psi_{n\mathbf{k}} | e^{-i(\mathbf{q}+\mathbf{G})\cdot\mathbf{r}} | \psi_{n'\mathbf{k}+\mathbf{q}} \rangle \\ &\times \langle \psi_{n'\mathbf{k}+\mathbf{q}} | e^{i(\mathbf{q}+\mathbf{G}')\cdot\mathbf{r}} | \psi_{n\mathbf{k}} \rangle \delta(\varepsilon_{n\mathbf{k}} - \varepsilon_{n'\mathbf{k}+\mathbf{q}} + \omega). \end{aligned} \quad (4)$$

In this case, a relevant numerical quantity is a broadening parameter [55,58] in the Gaussian representing the Dirac δ function. In this work, it was set to 50 meV. Indeed, employing a Gaussian with a finite thickness for the representation of the Dirac δ function poses a problem in the calculation of the intraband contribution to χ^{ol} since Gaussian is a symmetric function and is not required to vanish at $\omega = 0$. As a result, some spectral weight can be lost. To solve this problem, we multiply the Gaussian function by ω at low energies with corresponding modification of the normalization. Moreover, in such a way, the antisymmetry of χ^{ol} with respect to ω is ensured. The sampling of the 1BZ in Eq. (4) was performed

In the framework of the time-dependent density functional theory [50,51], χ is related to the density response function for noninteracting electrons χ^o via a Dyson-like equation $\chi = \chi^o + \chi^o(V + K^{\text{xc}})\chi$. Since for a periodic crystal all the quantities transform into matrices in reciprocal space, this integral equation takes a matrix form

$$\begin{aligned} \chi_{\mathbf{G}\mathbf{G}'}(\mathbf{q}, \omega) &= \chi_{\mathbf{G}\mathbf{G}'}^o(\mathbf{q}, \omega) + \sum_{\mathbf{G}_1} \sum_{\mathbf{G}_2} \chi_{\mathbf{G}\mathbf{G}_1}^o(\mathbf{q}, \omega) \\ &\times [V_{\mathbf{G}_1}(\mathbf{q})\delta_{\mathbf{G}_1\mathbf{G}_2} + K_{\mathbf{G}_1\mathbf{G}_2}^{\text{xc}}(\mathbf{q}, \omega)]\chi_{\mathbf{G}_2\mathbf{G}'}(\mathbf{q}, \omega). \end{aligned} \quad (2)$$

In Eq. (2), $K_{\mathbf{G}_1\mathbf{G}_2}^{\text{xc}}(\mathbf{q}, \omega)$ accounts for dynamical exchange-correlation effects. In this work, we present results obtained within the random-phase approximation (RPA), in which K^{xc} is set to zero. We have checked that the use of a so-called adiabatic local density approximation (ALDA) [50,52] for K^{xc} does not change the excitation spectra of the compounds under study significantly, in line with what was observed in the case of a pure graphite [53]. The main effect of the incorporation of the ALDA kernel on the excitation spectra consists in a moderate enhancement of the spectral weight of the features that already existed at the RPA level.

The Fourier coefficients $\chi_{\mathbf{G}\mathbf{G}'}^0(\mathbf{q}, \omega)$ can be calculated numerically using the following expression:

with the use of a $96 \times 96 \times 54$ grid for LiC_6 , a $96 \times 96 \times 30$ grid for SrC_6 , and a $90 \times 90 \times 30$ grid for BaC_6 . All the occupied (occ) and unoccupied (unocc) valence bands up to 40 eV above the Fermi level were included. Subsequently, having evaluated the imaginary part, the real part of the $\chi_{\mathbf{G}\mathbf{G}'}^0(\mathbf{q}, \omega)$ matrix elements is obtained via the Hilbert transform using an energy cutoff of 40 eV. The local field effects (LFEs) are included in the evaluation of the energy-loss function through the incorporation in Eq. (2) of the nondiagonal matrix elements [59,60].

III. CALCULATION RESULTS AND DISCUSSION

A. Band structure

The calculated electronic band structure of LiC_6 , SrC_6 , and BaC_6 in the vicinity of the Fermi level along the high-symmetry directions of the 1BZ is reported in Fig. 2. Overall it is in good agreement with the previous results [7,8,29–31,61]. Figure 2 demonstrates that the intercalation process produces notable changes in the energy bands of a pure graphite. In particular, one can observe an almost rigid downward shift of the bonding π and antibonding π^* carbon-derived bands by about 0.9 eV in LiC_6 , 1.8 eV in SrC_6 , and 1.7 eV in BaC_6 in comparison with a pure graphite. As a result, the π^* bands become partly occupied in all the cases, unlike for pure graphite where they are almost empty. There is no significant

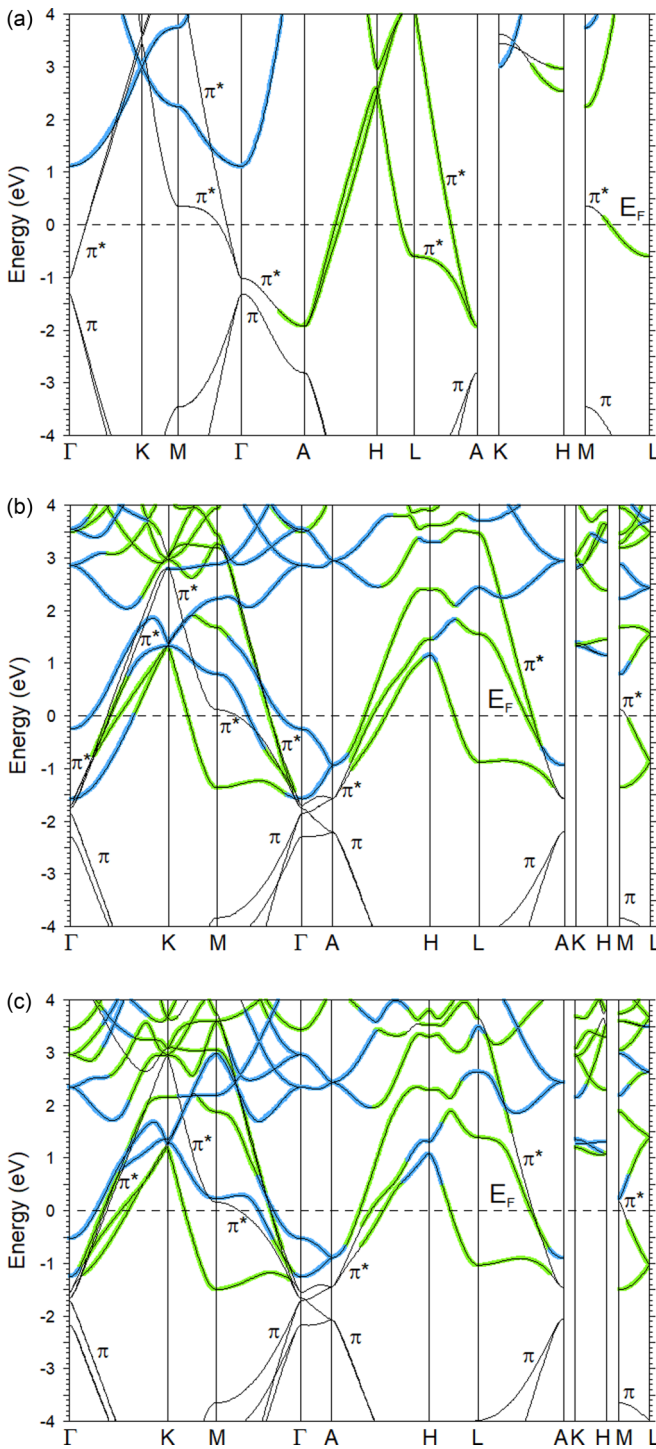


FIG. 2. Calculated band structure of (a) LiC_6 , (b) SrC_6 , and (c) BaC_6 along high-symmetry directions of the 1BZ. The interlayer and hybridized bands [31] are highlighted with blue and green, respectively. The Fermi level located at the zero energy is shown by a horizontal dashed line.

modification in the dispersion of these π and π^* bands due to the presence of the intercalant atoms.

Additionally, the location of the intercalant atoms between the carbon atomic layers brings an interlayer band (highlighted with blue) closer to the Fermi level. In LiC_6 , this

band appears totally unoccupied and its bottom at the Γ point is located around 1.1 eV above the Fermi level, in agreement with the previous calculations [7,8]. In SrC_6 and BaC_6 , the interlayer band appears to be partly occupied. In these compounds, the bottom of this band is located at the Γ point at energies of 1.56 and 1.25 eV below the Fermi level, respectively. It can be compared with its energy position at -1.25 eV in CaC_6 [39,61]. Such an energy position of the interlayer band reflects a smaller charge transfer from the intercalant to the carbon layers in CaC_6 and BaC_6 in comparison to SrC_6 . Note that in SrC_6 and BaC_6 along the ΓA symmetry direction, this band is totally occupied. The top of this band is located at the Γ point at energies of -0.25 and -0.53 eV, respectively. On the contrary, in CaC_6 along the ΓA direction such a band is semioccupied, reaching a maximal energy of 0.7 eV at the A point [39]. The resulting narrowing of the interlayer band upon the increase of the intercalant atomic number correlates with the increase of the interlayer spacing, as is evident from Table I.

In all these systems, one can find the hybridized π^* bands (highlighted in Fig. 2 with green). These hybridized π^* bands are derived from the corresponding graphite bands whose dispersion is notably modified due to the presence of the intercalant. This means that BaC_6 and SrC_6 exhibit three kinds of energy bands crossing the Fermi levels, namely antibonding carbon π^* bands, interlayer bands, and hybridized π^* bands with strong charge density in the interlayer region [31]. Thus, the low-energy electronic dynamics becomes enriched due to the presence of these carriers near the Fermi level, as it is demonstrated below. In the case of LiC_6 , the dynamics at the Fermi surface is determined by two kinds of carriers in the carbon π^* bands and the hybridized π^* bands.

Since graphite is gapless at the K point, a remarkable effect of the intercalation is the appearance of an energy gap of 0.29, 0.14, and 0.09 eV at the Γ point (a back-folded K point in the 1BZ of the graphite) for LiC_6 , SrC_6 , and BaC_6 , respectively. As seen in Figs. 2(b) and 2(c), the intercalation of Sr and Ba atoms into graphite brings about the d and f electronic states, which are totally unoccupied and reside at energies above ~ 1.5 and ~ 1 eV, respectively. Note that in this work, the electronic structure was calculated in the scalar-relativistic approach. We do not expect that the inclusion of spin-orbit coupling might introduce significant variation in the excitation spectra in these materials since it is known that, for instance, in the case of most heavy Ba, the changes in the bulk electronic structure caused by the spin-orbit interaction do not exceed 0.2 eV in the unoccupied part. The states at the Fermi level and below are not modified notably by the spin-orbit interaction at all [62].

The main effects caused by the intercalation process in the materials under study here are summarized below in comparison with pure graphite. The first effect consists in charge transfer taking place from the intercalant atoms to the carbon layers, which is evidenced through the filling of the π^* band (an almost empty band in graphite). The second is the formation of an energy gap between the π and π^* bands at the Γ point. The third is the downward shift of the parabolic-like dispersing interlayer band in these three systems.

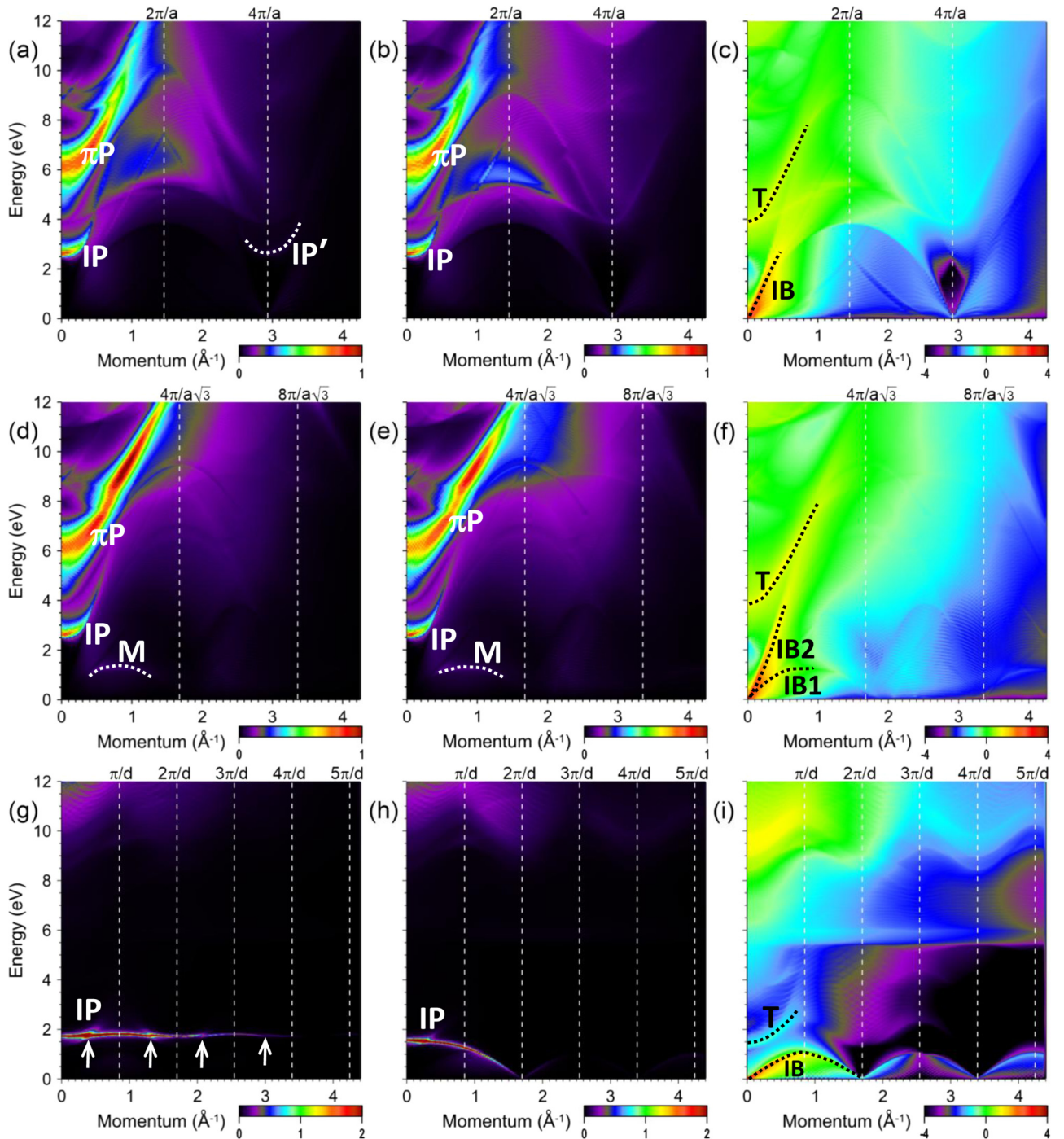


FIG. 3. Loss function, $L(\mathbf{Q}, \omega)$, of LiC_6 at momentum transfers \mathbf{Q} along the a^* axis calculated (a) with and (b) without inclusion of the local-field effects. The respective $\log_{10}\{\text{Im}[\epsilon]\}$ is shown in (c). In (d), (e), and (f) and in (g), (h), and (i) the same quantities are presented for \mathbf{Q} 's directed along the b^* and c^* axes, respectively. Peaks in the loss function corresponding to the π and intraband plasmons are labeled by πP and IP , respectively. In (a) the peak corresponding to an intraband plasmon reappearing at large momentum transfers is denoted as IP' . Peak M in (d) and (e) is discussed in the text. In (c), (f), and (i) the peaks in $\text{Im}[\epsilon]$ generated by the intraband transitions are labeled as IB , $IB1$, and $IB2$. A clear peak in $\text{Im}[\epsilon]$ produced by the interband transitions is denoted as T . The dispersion of all these peaks is highlighted by white and black dotted lines. In (g) vertical arrows point to regions where there is enhanced hybridization of the IP mode with the T peak in $\text{Im}[\epsilon]$.

B. Dielectric properties

I. LiC_6

The excitation spectra of LiC_6 in the energy range of 0–12 eV are presented in Fig. 3. Panels (a), (d), and (g)

show the loss function $L(\mathbf{Q}, \omega)$ as a function of energy ω and momentum transfer \mathbf{Q} directed along the a^* , b^* , and c^* axes, respectively. These data are obtained with the inclusion of the LFEs. Notice that the magnitude of momentum transfer \mathbf{Q} can exceed the size of the 1BZ since $\mathbf{Q} = \mathbf{q} + \mathbf{G}$, where vector

\mathbf{q} belongs to the 1BZ and \mathbf{G} is a reciprocal-lattice vector bringing \mathbf{Q} into the 1BZ.

Inspection of Figs. 3(a), 3(d), and 3(g) reveals that in LiC_6 there are several spectral features in this energy range. Furthermore, the anisotropy of the dielectric properties in this material is evident. In particular, along the c^* direction the spectrum is remarkably different from that in the basal a^*-b^* plane. It is consistent with a weak interaction between the carbon atomic layers in this material.

At momentum transfers in the a^*-b^* plane, a feature dominating the spectra is labeled as πP and can be seen in the upper-energy region of Figs. 3(a) and 3(d). It shows a parabolic-like positive dispersion upon momentum transfer increase in both a^* and b^* symmetry directions. The πP mode has an energy of ~ 6.2 eV at small $Q_{\parallel a^*, \parallel b^*}$ values and disperses upward to energies exceeding 12 eV at large momentum transfers. The energy of this spectral feature at $Q = 0$ is in good agreement with a value $\omega_{\pi\text{P}} = 6.3$ eV measured for LiC_6 in the EELS experiment by Grunes *et al.* [63] and later analyzed by Chen and Rabii [64]. In LiC_6 , the energy of the πP mode at momentum transfers in the a^*-b^* plane is significantly shifted downward in comparison to a pristine graphite. Such a mode was reported initially in graphite, where it appears at $\omega \sim 7$ eV in the optical limit [65,66]. It is interpreted as the collective oscillation of the electron charge residing in the π energy bands. Later on it was observed in other GICs at lower energies [65,67–71]. In particular, a first-principles calculation [39] and an EELS measurement [40] have found a similar parabolic-like dispersion as well as an energy downward shift for the πP mode in graphite intercalated with Ca.

A similar πP peak in the loss function was found in a single carbon monolayer—graphene. There was intense discussion [72–74] about whether such a peak in the loss function of graphene is a signature of collective excitation or not. In the bulk electron system, the condition for the existence of collective excitation—plasmon—is $\epsilon(\mathbf{Q}, \omega) = 0$ [75]. However, in real materials such a condition is almost never realized. Therefore, in this work we use the less stringent definition of bulk collective excitation [76]: for a bulk mode to exist at a certain energy, three conditions should be fulfilled: (i) there is a clear peak in the loss function, (ii) $\text{Re}[\epsilon]$ is zero or close to zero, and (iii) $\text{Im}[\epsilon]$ presents a local minimum. To answer this question in the case of LiC_6 , in Fig. 4 we report the dielectric and loss functions calculated at $Q_{\parallel a^*} = 0.03 \text{ \AA}^{-1}$. One can see that all three of the above conditions are fulfilled in the πP case. One of the zero-crossings in $\text{Re}[\epsilon]$ occurs at an energy of 5.7 eV, i.e., very close to the energy position of the πP peak in the loss function. Also the imaginary part of ϵ has a shallow local minimum at almost the same energy region. This confirms the true plasmonic nature of the πP mode in LiC_6 . Note that in the dielectric function derived from the EELS measurements in Ref. [63], the real part does not cross the zero line in the nearby energy window. Instead, $\text{Re}[\epsilon]$ has a local minimum of ≈ 0.15 at $\omega = 5.4$ eV. We attribute this discrepancy to uncertainty in the determination of the dielectric function from the measured loss function.

Although the calculated πP peak dispersion is rather similar along the a^* and b^* directions, some notable differences

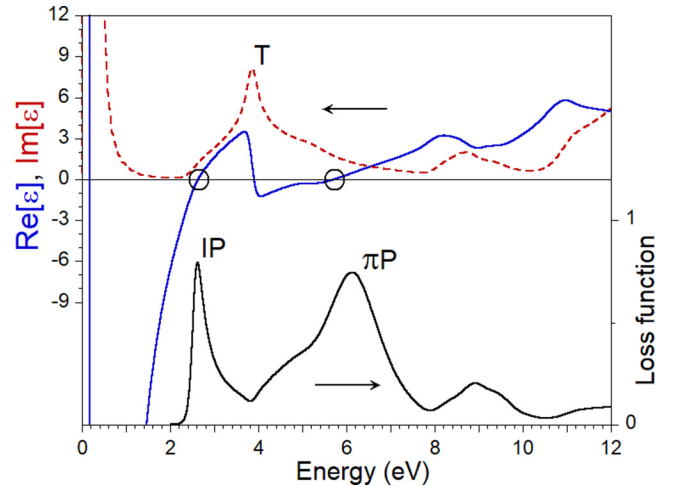


FIG. 4. Upper panel: Real $\text{Re}[\epsilon]$ (blue solid line) and imaginary $\text{Im}[\epsilon]$ (red dashed line) parts of the dielectric function in LiC_6 at $Q_{\parallel a^*} = 0.03 \text{ \AA}^{-1}$. Lower panel: Corresponding loss function evaluated with the inclusion of LFEs (black solid line). Peaks in the loss function corresponding to the intraband and π plasmons are marked as IP and πP , respectively.

can be detected. Thus, while the intensity of this mode in Fig. 3(a) is greatly reduced when it reaches energies around 10 eV, in Fig. 3(d) it is still present as a well-defined feature in this energy region. A detailed comparison of Figs. 3(a) and 3(d) also reveals that the πP peak dispersion presents a certain anisotropy in the basal plane that is steeper in the a^* direction. In the loss function of Fig. 4 we observe a broad peak centered at an energy of 8.9 eV. Its presence is explained by the existence in $\text{Im}[\epsilon]$ of the interband peak around 8.7 eV. Due to the close proximity of the energy position of these two peaks and the absence of a zero-crossing in $\text{Re}[\epsilon]$ in the nearby energy region, we interpret this peak in the loss function as interband transitions. In Figs. 3(a) and 3(d) it is seen that the dispersion of this peak is positive and can be detected up to $Q \sim 0.3 \text{ \AA}^{-1}$.

The next feature in the loss function at momentum transfers in the a^*-b^* plane appears at lower energy. It is the intraband plasmon, and the corresponding peak in the calculated $L(\mathbf{Q}, \omega)$ is labeled as IP. Its energy at small $Q_{\parallel a^*, \parallel b^*}$'s is 2.6 eV. The collective character of this feature in the loss function is confirmed by the behavior of the real and imaginary parts of the dielectric function at $Q_{\parallel a^*} = 0.03 \text{ \AA}^{-1}$ presented in Fig. 4. Here one can see that at energies around ω_{IP} , $\text{Re}[\epsilon]$ crosses the zero line with a positive derivative and $\text{Im}[\epsilon]$ is rather small. In the EELS experiment performed by Grunes *et al.* [63] in LiC_6 , a value of $\omega_{\text{IP}} = 2.85$ eV at $Q \sim 0.1 \text{ \AA}^{-1}$ for the intraband plasmon energy was reported. This value is in good agreement with $\omega_{\text{IP}} = 2.8$ eV obtained in our calculations at the same in-plane momentum transfer. Additionally, at small momentum transfers we observe a good agreement between our results and the energy of the IP mode reported by Fischer *et al.* [77] and Basu *et al.* [78] in reflectivity experiments.

In LiC_6 a sharp and narrow IP peak exhibits a parabolic-like positive dispersion. This mode disperses up to $\omega \sim 4$ eV at $Q_{\parallel a^*} = 0.45 \text{ \AA}^{-1}$ and to $\omega \sim 5.5$ eV at $Q_{\parallel b^*} = 0.65 \text{ \AA}^{-1}$.

Such behavior of the IP mode in LiC_6 is strikingly different from what occurs, e.g., in CaC_6 , where a similar mode possesses a negative dispersion [39]. The sharpness and positive dispersion of the IP mode peak in LiC_6 can be understood inspecting $\text{Im}[\epsilon]$ shown in Figs. 3(c) and 3(f). One can see that the IP peak propagates in the momentum-energy phase space where there is a local pseudogap in $\text{Im}[\epsilon]$ located between the intraband IB (IB2) peak and the interband one T with an energy of 3.8 eV at $Q_{\parallel a^*, \parallel b^*} = 0$. Moreover, the interband peak T has strong upward dispersion upon a momentum transfer increase, contrary to its almost flat dispersion in the case of CaC_6 [39]. Once the IP mode dispersion reaches the upper border of the intraband electron-hole continuum, its dispersion increases sharply. However, this is accompanied by a quick reduction of the IP peak spectral weight in the loss function. Finally, at certain momentum transfers reported above this mode ceases to exist.

In Figs. 3(b) and 3(e) we present $L(\mathbf{q}, \omega)$ calculated without inclusion of the LFEs for \mathbf{Q} 's along the a^* and b^* symmetry directions, respectively. From a comparison with the loss functions given in Figs. 3(a) and 3(d), one can conclude that the LFEs play a negligible role in the formation of the excitation spectra in LiC_6 at momentum transfers in the carbon basal plane. The only visible effect, besides some variation in intensity in certain regions of the momentum-energy phase space, consists in the reappearance of the IP mode in the vicinity of $Q_{\parallel a^*} = 4\pi/a$. In Fig. 3(a) we denote this weak peak as IP' and mark its dispersion by a white dotted line. An analysis of the dielectric function behavior confirms that this feature cannot be considered as collective excitation.

As seen in Fig. 3(g), the response properties of LiC_6 along the c^* direction differ dramatically from that in the basal a^*-b^* plane. The most visible difference is a lack of the π P mode along this direction. Instead, in the excitation spectrum at the c^* direction one can observe a wide featureless pseudogap at energies above ~ 2 eV. Similarly, a structureless spectrum along this momentum transfer direction was reported in pristine graphite [53,79]. Its presence in $L(\mathbf{q}, \omega)$ can be explained by the rather featureless behavior of $\text{Im}[\epsilon]$ presented in Fig. 3(i), where the large portion of the momentum-energy phase space is almost free of the interband transitions.

The peculiar feature of the loss function in the c^* symmetry direction is the presence of the IP mode at lower energies (by about 1 eV lower in comparison to the a^*-b^* plane), as can be seen in Fig. 3(g). This narrow and sharp feature shows the longest lifetime and highest intensity in the spectrum along this direction. At small $Q_{\parallel c^*}$'s the energy of this feature is around 1.7 eV. Upon an increase in momentum transfer, the IP mode exhibits almost flat dispersion over subsequent BZs with a variation in energy less than 0.1 eV. Its presence in the loss function can be traced up to momentum transfers close to $Q_{\parallel c^*} = 4\pi/c$. An analysis of the IP plasmon dispersion in Fig. 3(g) reveals that in certain regions marked by vertical white arrows, it experiences some distortions. Such behavior can be explained by the presence of a well-defined peak T in $\text{Im}[\epsilon]$ of Fig. 3(i) produced by the interband transitions. As a result, in these regions the IP plasmon can decay more efficiently into the electron-hole pairs. One can see in Fig. 3(h) that without inclusion of the LFEs, the IP peak has

pronounced negative dispersion and eventually reaches a zero energy at $Q_{\parallel c^*} = 2\pi/d$. By incorporating the LFEs in the calculation of the loss function, the IP dispersion transforms into the almost flat one observed in Fig. 3(g). Such influence of the LFEs on the dispersion of the IP mode in LiC_6 is rather unique since in the previously studied materials the variation of the IP plasmon energy upon propagation into the subsequent BZ's was significant [80–83]. On the other hand, a rather flat plasmon dispersion over an extended momentum transfer range was found in the electride Ca_2N [84]. However, in that case the IP dispersion is not discontinuous.

A detailed inspection of the low-energy region of the spectrum of LiC_6 confirms that in this compound at energies below ~ 1.5 eV there is not any plasmon feature. This is opposite to the Li-doped graphene case in which a low-energy AP mode was predicted to exist [85]. Such an opposite trend is explained by the fact that in the Li-doped graphene, the free-like interlayer energy band is partly occupied, whereas in the bulk LiC_6 it is located totally above the Fermi level. The only feature in this energy range can be detected in the loss function of Fig. 3(d) and is labeled as M . Along the b^* direction its presence can be detected in the $0.4\text{--}1.3 \text{ \AA}^{-1}$ momentum transfer interval. It has a maximum at an energy of 1.3 eV and disperses down to an energy of about 0.8 eV. Since it can also be seen in the loss function of Fig. 3(e), we deduce that the LFEs do not alter its properties. An analysis of the dielectric function shows that $\text{Re}[\epsilon]$ does not approach the zero line at energies around the M peak. Hence it cannot be classified as a collective excitation. Indeed, the energy position of this peak in the loss function is very close to the IB1 peak location in $\text{Im}[\epsilon]$ shown in Fig. 3(f). This confirms the single-particle nature of the M peak in the loss function.

The rather featureless behavior of the low-energy excitation spectrum in LiC_6 is consistent with its band structure, with the interlayer band being totally unoccupied and only two kinds of carbon-derived states present at energies near the Fermi level, as seen in the density of states (DOS) distribution presented in Fig. 5. In the DOS of Fig. 5(a) one can detect a local peak P1 with group velocity in the a^* direction about 0.18 a.u. at the Fermi level. Another local peak P2 at E_F can be found in the DOS reported in Fig. 5(a) at $v_{\parallel a^*} = 0.32$ a.u. However, despite the presence of two groups (apart from a trivial peak with zero velocity that does not produce any separate peak in $\text{Im}[\epsilon]$) of states with different group velocities at the Fermi level, in $\text{Im}[\epsilon]$ of Fig. 3(c) we only observe one dominating IB peak mostly linked to the P2 peak in the DOS. Apparently, the contribution to $\text{Im}[\epsilon]$ from the P1 peak decays very quickly upon momentum transfer increase and can only be seen in Fig. 3(c) as a shoulder on the low-energy side of the IB peak. Under these conditions, an acoustic plasmon cannot exist. In the b^* direction, the DOS of Fig. 5(b) has two peaks P1 and P2 at the Fermi level at velocities of 0.22 and 0.38 a.u., respectively. As a result, two intraband peaks IB1 and IB2 can be found in $\text{Im}[\epsilon]$ of Fig. 3(f). Nevertheless, the presence of two intraband peaks in $\text{Im}[\epsilon]$ does not lead to the appearance in the loss function of an additional plasmon peak with a soundlike dispersion. Actually, the presence of two intraband peaks in $\text{Im}[\epsilon]$ does not guarantee the existence of such a mode. In reality, a delicate balance between their

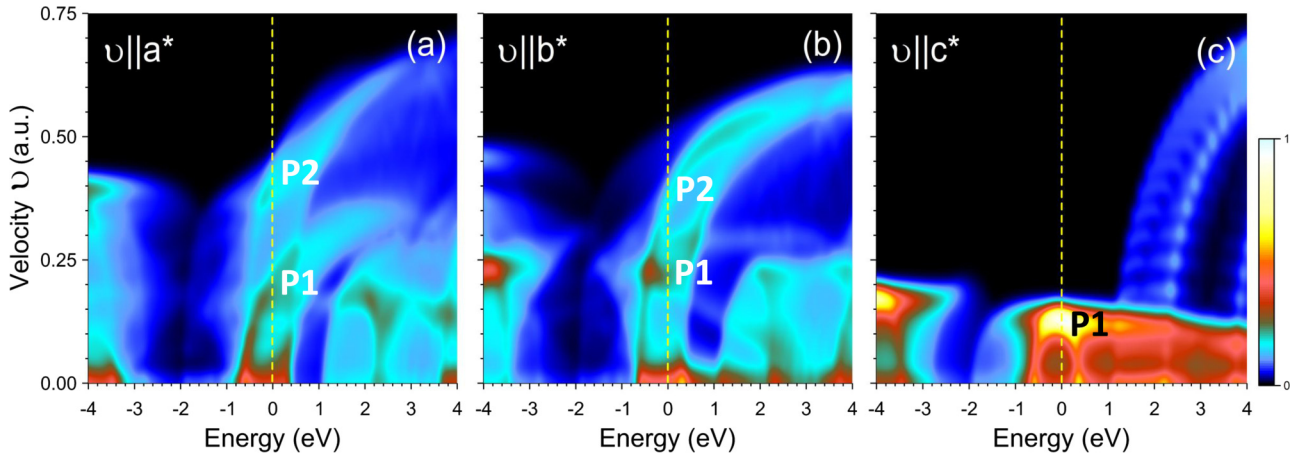


FIG. 5. Density of states distribution in LiC_6 vs energy and group velocity components along (a) a^* , (b) b^* , and (c) c^* symmetry directions. Peaks at the Fermi level are labeled as P1 and P2. The energies are relative to the Fermi level set to zero.

mutual energetic positions and strengths definitely determines whether this kind of plasmon can be realized or not [86].

When momentum transfer occurs in the c^* direction, it is even more evident that an AP cannot be realized in this direction since in the DOS of Fig. 5(c) one peak P1 at $v_{\parallel c^*} = 0.18$ a.u. can be found on the Fermi surface only. It generates a single intraband peak IB in $\text{Im}[\epsilon]$ of Fig. 3(i) resulting in the situation of a conventional one-component electron gas scenario [87] where an AP mode is impossible.

2. SrC_6

In Fig. 6 we show the excitation spectra of SrC_6 along three main symmetry directions of the hexagonal lattice. Several features can be found in Figs. 6(a), 6(d), and 6(g), where the loss function calculated with the inclusion of the LFEs along the a^* , b^* , and c^* directions is given. By inspecting the spectra along all symmetry directions, a strong anisotropic dielectric response in SrC_6 is evident in correspondence with what is found in LiC_6 and CaC_6 [39].

In the upper energy region of the calculated loss function in the a^* - b^* plane presented in Figs. 6(a) and 6(d), the π P mode appears at lower energies than a similar mode in a pure graphite but at slightly higher energies than in LiC_6 . This feature exhibits the highest intensity in the spectra and shows positive parabolic-like dispersion along both in-plane symmetry directions. This mode disperses from $\omega_{\pi P} \approx 6.4$ eV at small $Q_{\parallel a^*}, \parallel b^*$'s to $\omega_{\pi P} \approx 13$ eV at $Q_{\parallel a^*} = 1.4 \text{ \AA}^{-1}$ and to $\omega_{\pi P} \approx 14$ eV at $Q_{\parallel b^*} = 1.7 \text{ \AA}^{-1}$. One can note that in the loss function of Figs. 6(a) and 6(d) the π P peak is notably broader in comparison with the same peak in LiC_6 . This can be understood comparing $\text{Im}[\epsilon]$ of Figs. 6(c) and 6(f) with that of Figs. 3(c) and 3(f) for LiC_6 . One can find that in the case of SrC_6 in the region where the π P mode exists, $\text{Im}[\epsilon]$ has a broad peak generated by efficient interband transitions. Moreover, the number of such transitions in SrC_6 is apparently larger, even in comparison with CaC_6 studied in Ref. [39]. This can be explained by the presence of the unoccupied Sr d states in the band structure of SrC_6 in Fig. 2(b). The impact of the interband transitions involving these states in SrC_6 is so strong that indeed the π P peak is split into a

two-peak structure with a weaker second peak at an energy of $\omega \approx 5.3$ eV at vanishing $Q_{\parallel a^*}$ and $Q_{\parallel b^*}$. As seen in Figs. 6(a) and 6(d) upon increasing momentum transfer, this satellite peak disperses upward in concert with a main π P peak.

The next prominent spectral feature in the a^* - b^* plane is the intraband plasmon mode IP appearing at lower energies. It has negative dispersion [going to lower energy values as $Q_{\parallel a^*}$ ($Q_{\parallel b^*}$) increases] starting at an energy of 3.65 eV at small $Q_{\parallel a^*}, \parallel b^*$ to around 3.5 eV (3.6 eV) at $Q_{\parallel a^*} = 0.4 \text{ \AA}^{-1}$ ($Q_{\parallel b^*} = 0.3 \text{ \AA}^{-1}$). The relative narrowness of the IP peak and confinement to the small momentum transfer region can be explained by the fact that it resides in the upper part of a local energy gap between the intraband IB2 and the interband T peaks in $\text{Im}[\epsilon]$ shown in Figs. 6(c) and 6(f). Once the IP peak reaches the upper border of the intraband electron-hole continuum region IB2, it becomes heavily Landau-damped and disappears. The initial negative dispersion of the IP mode is related to the shape of the gap region in $\text{Im}[\epsilon]$ of Figs. 6(c) and 6(f) where the interband transition region borders at the bottom have almost flat dispersion at small momentum transfers, as occurs in CaC_6 [39].

In the loss function of Fig. 6(a) at finite momentum transfers in the 3.0–3.5 eV energy range, one can detect a peak K . In the case of Fig. 6(d) we find two similar peaks $M1$ and $M2$. An analysis of the dielectric function behavior in the nearby energies demonstrates that all these peaks do not represent collective excitations.

From a comparison of Figs. 6(a) and 6(d) with Figs. 6(b) and 6(e), where $L(\mathbf{Q}, \omega)$ calculated without inclusion of the LFEs is reported, one can obtain information about the relevance of the LFEs in the basal plane. From such a comparison, some impact of the LFEs on the excitation spectra in SrC_6 can be noted. Thus the intensity of the π P peak is enhanced upon inclusion of the LFEs. Moreover, the LFEs are responsible for the appearance of the K ($M1$ and $M2$) loss peaks at momentum transfers along the a^* (b^*) direction. On the other hand, the LFEs greatly suppress the intensity of peak K existing in the loss function of Fig. 6(b) at energies between 5.0 and 5.5 eV. The effect is so strong that in the loss function of Fig. 6(a) its presence can be hardly detected.

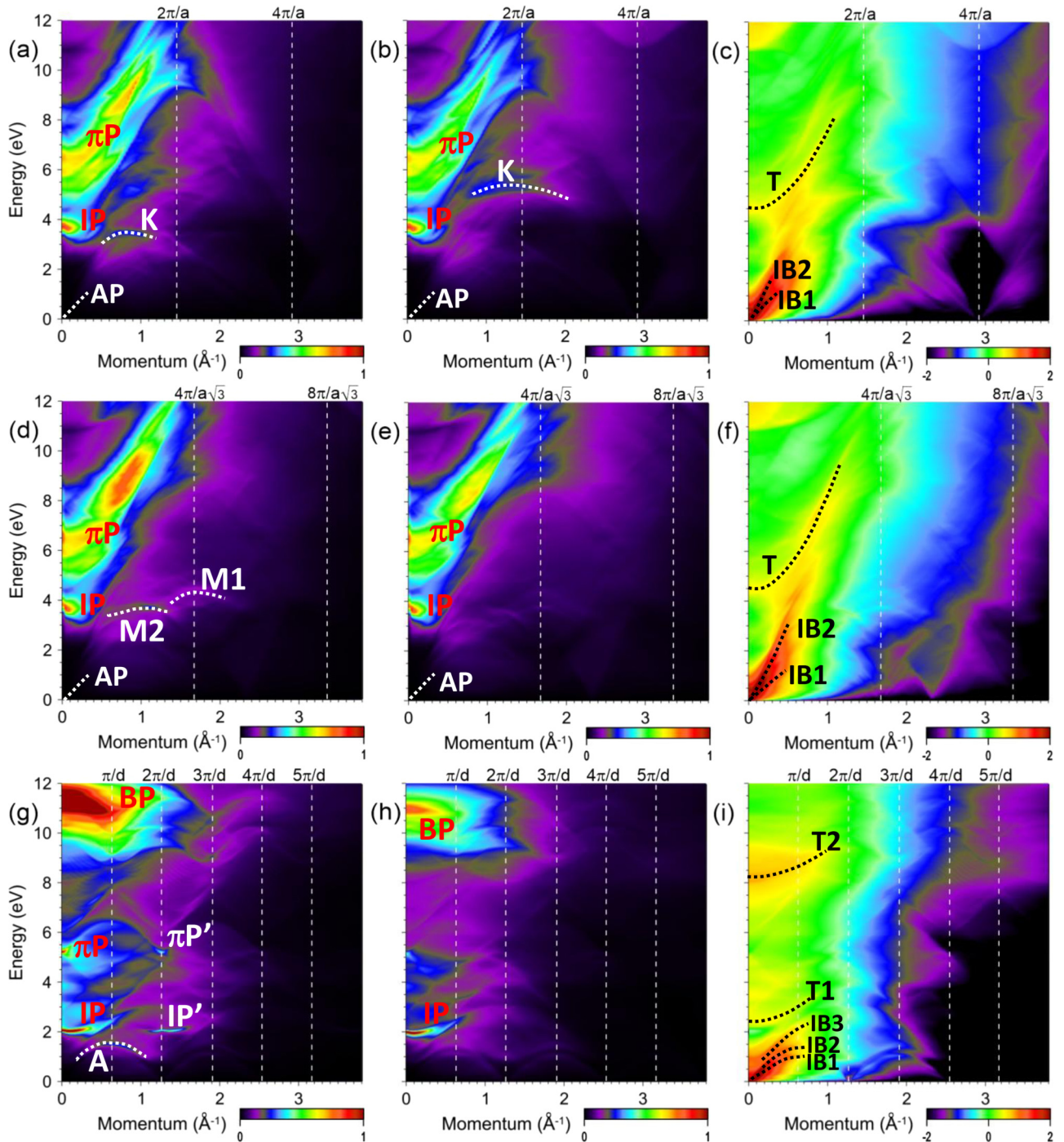


FIG. 6. Loss function, $L(\mathbf{Q}, \omega)$, of SrC_6 at momentum transfers \mathbf{Q} along the a^* axis calculated (a) with and (b) without inclusion of the local-field effects. The respective $\log_{10}\{\text{Im}[\epsilon]\}$ is shown in (c). In (d), (e), and (f) and in (g), (h), and (i) the same quantities are presented for \mathbf{Q} 's directed along the b^* and c^* axes, respectively. Peaks in the loss function corresponding to the bulk, π , intraband, and acoustic plasmons are labeled by symbols BP, πP , IP, and AP, respectively. The peaks K , $M1$, $M2$, $\pi P'$, IP' , and A are discussed in the main text. Dispersion of weak peaks in the loss function is highlighted by white dotted lines. In (c), (f), and (i) the peaks in $\text{Im}[\epsilon]$ generated by the intraband transitions are labeled as IB, IB1, and IB2, whose dispersion as well as that of the interband T peak is highlighted by black dotted lines.

Additionally, in the lower energy region of the spectra in the a^* - b^* plane, a weak feature can be detected. In Figs. 6(a) and 6(d) its dispersion is highlighted by a white dotted line and labeled AP. The AP peak disperses linearly from zero energy at vanishing momentum transfer to $\omega_{\text{AP}} \approx 1.0$ eV at $Q_{\parallel a^*} \approx 0.3 \text{ \AA}^{-1}$. The AP mode is an acoustic plasmon whose

properties can be seen in more detail in Fig. 7. Here the real and imaginary parts of the dielectric function and the loss function are presented, as an example, at momentum transfer $Q_{\parallel a^*} = 0.12 \text{ \AA}^{-1}$. At $\omega = 0.47$ eV the real part of the dielectric function $\text{Re}[\epsilon]$ reaches zero and remains on the negative side until $\omega = 0.56$ eV where it becomes positive

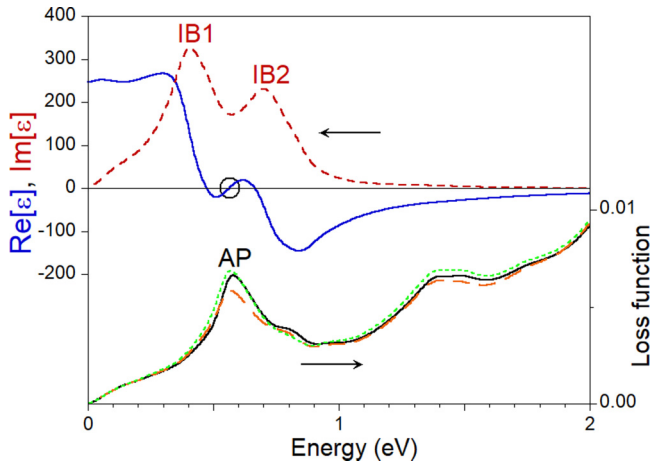


FIG. 7. Upper panel: Real (blue solid line) and imaginary (red dashed line) parts of the dielectric function in SrC₆ evaluated at momentum transfer $Q_{\parallel a^*} = 0.12 \text{ \AA}^{-1}$. The intraband peaks in $\text{Im}[\epsilon]$ generated by the slow and fast carriers at the Fermi level are labeled as IB1 and IB2, respectively. The second zero-crossing of $\text{Re}[\epsilon]$ caused by the presence of two intraband peaks in $\text{Im}[\epsilon]$ is highlighted by an open circle. Lower panel: Loss function with (black solid line) and without (orange long-dashed line) inclusion of the LFEs evaluated with the RPA kernel. The TDDFT result is shown by a green dotted line. The peak in the loss function labeled as AP corresponds to the acoustic plasmon.

again. Using a peak AP in the loss function at $\omega = 0.56 \text{ eV}$ combined with the local minimum of the $\text{Im}[\epsilon]$ at almost the same energy, we can interpret this feature as a collective electronic excitation. Since the energy position of the IB1 and IB2 peaks in $\text{Im}[\epsilon]$ has a linear dependence on the magnitude of the momentum transfer, eventually the energy of the AP mode goes to zero with the reduction of Q_{a^*} . We verify a similar structure in the low-energy domain for the dielectric function along the b^* direction, which confirms that the AP is realized in the basal plane.

To understand the origin of a two-peak structure in $\text{Im}[\epsilon]$ at small $Q_{\parallel a^*}$'s and $Q_{\parallel b^*}$'s, we analyze in Figs. 8(a) and 8(b)

the DOS distribution for electronic states with group velocity components in the a^* and b^* directions, respectively. One can see that at the Fermi level a notable peak P1 appears in both figures at $v_{\parallel a^*} = 0.20 \text{ a.u.}$ and $v_{\parallel b^*} = 0.22 \text{ a.u.}$, respectively. A second weaker peak P2 can be found on the Fermi surface at $v_{\parallel a^*} = 0.39 \text{ a.u.}$ and $v_{\parallel b^*} = 0.35 \text{ a.u.}$ This two-peak structure in the DOS at the Fermi level transforms into a two-peak structure in $\text{Im}[\epsilon]$ at small momentum transfers, which may generate an acoustic plasmon. Nevertheless, the strength of the AP peak in SrC₆ is rather low. As Fig. 7 confirms, its width is rather large, resulting in the short lifetime of the AP excitation. In the case of Fig. 7, the weakness of the AP can be explained by the small difference between the energy positions of the peaks IB1 and IB2 in $\text{Im}[\epsilon]$. Such positions lead to the relatively large amplitude of $\text{Im}[\epsilon]$ in the region between them, where $\text{Re}[\epsilon]$ crosses the zero line with a positive energy derivative. The large value of $\text{Im}[\epsilon]$ and relatively small derivative of $\text{Re}[\epsilon]$ in the nearby region determine the efficient decay of the AP into electron-hole pairs.

Note that the AP peak appears in the loss function of Figs. 6(b) and 6(e) obtained without inclusion of the LFEs. For illustration, in Fig. 7 we add an orange long-dashed line demonstrating this loss function at $Q_{\parallel a^*} = 0.12 \text{ \AA}^{-1}$. One can see that the LFEs only slightly modify the shape and the energy position of the AP peak in the loss function. Additionally, we demonstrate (green dotted line) that the dynamical exchange correlations beyond the RPA bring the AP energy close to that obtained without LFEs, in such a way that it partly compensates for the LFEs. Nevertheless, one can conclude that both the LFEs and the exchange-correlations play a modest role in the formation of the AP peak properties.

The loss function of SrC₆ at momentum transfers along the c^* symmetry direction is reported in Fig. 6(g). In contrast to LiC₆, it presents a richer structure in this energy range. On the upper energy side at $Q_{\parallel c^*}$'s smaller than 1.8 \AA^{-1} , we observe a dominant peak BP corresponding to the bulk plasmon. Its energy at $Q_{\parallel c^*} = 0$ is 11.1 eV , which can be explained by the presence of a prominent interband peak T2 in $\text{Im}[\epsilon]$ of Fig. 6(i) centered at $\omega = 8.2 \text{ eV}$ at small $Q_{\parallel c^*}$'s. The width of the BP peak in the loss function is about 1 eV .

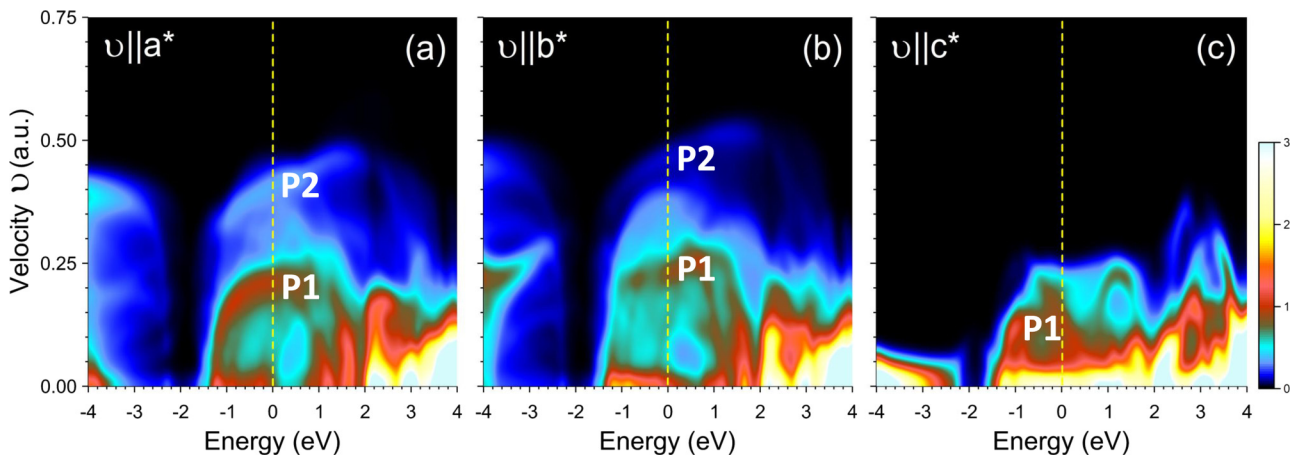


FIG. 8. Density of states distribution in SrC₆ vs energy and group velocity components along (a) a^* , (b) b^* , and (c) c^* symmetry directions. Peaks at the Fermi level are labeled as P1 and P2. The energies are relative to the Fermi level set to zero.

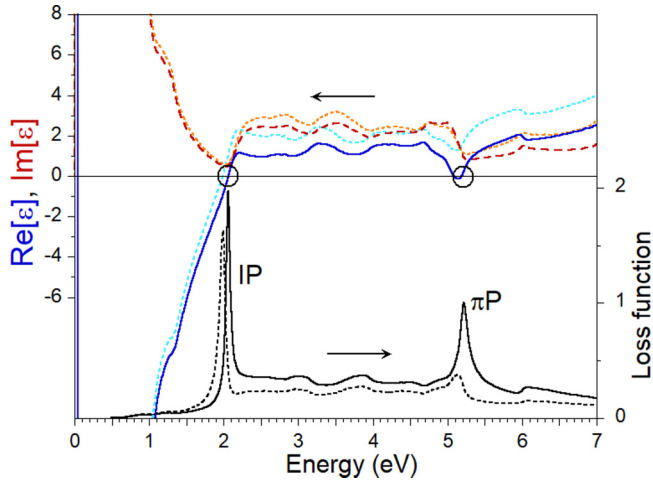


FIG. 9. Upper panel: Real (blue solid line) and imaginary (red dashed line) parts of the dielectric function in SrC₆ evaluated at momentum transfer $Q_{\parallel c^*} = 0.02 \text{ \AA}^{-1}$ with the inclusion of the LFEs. The same quantities obtained without LFEs are shown by cyan and orange dotted lines, respectively. The zero-crossings of $\text{Re}[\epsilon]$ confirming the collective nature of the πP and IP loss peaks are highlighted by open circles. Lower panel: Loss function with (black solid line) and without (black dotted line) inclusion of the LFEs. The π and intraband plasmon peaks are labeled as πP and IP, respectively.

With a momentum transfer increase, the BP peak presents a negative dispersion reaching a minimum energy of $\approx 10.6 \text{ eV}$ at $Q_{\parallel c^*} = 0.8 \text{ \AA}^{-1}$. At larger momentum transfers, the BP peak splits into several branches and it is difficult to follow it. Comparing the loss function in Figs. 6(g) and 6(h), we conclude that the LFEs have a notable impact on the BP peak shape. In particular, its strength increases considerably upon taking into account the LFEs. Moreover, the LFEs push the BP peak energy position slightly upward. In particular, at $Q_{\parallel c^*} = 0$ its energy is increased due to the LFEs by about 0.2 eV .

In general, the LFEs significantly modify the loss function in SrC₆ at momentum transfers along the c^* direction, as can be deduced from a comparison of Figs. 6(g) and 6(h), where $L(Q_{\parallel c^*}, \omega)$ calculated, respectively, with and without inclusion of the LFEs is reported. In Fig. 6(g) one can observe a significant enhancement of all the peaks and the appearance of some new ones in comparison with Fig. 6(h).

From Fig. 6(g) we confirm the presence of a weak πP peak along the c^* direction in SrC₆ contrary to what occurs in a pure graphite [53,79] and in LiC₆. However, such a peak is almost invisible in the loss function of Fig. 6(h) obtained without taking into account the LFEs. To clarify the situation, in Fig. 9 we present the dielectric and loss functions evaluated at $Q_{\parallel c^*} = 0.02 \text{ \AA}^{-1}$. In this figure, one can see that indeed the πP peak appears in the loss function upon the inclusion of the LFEs only. Moreover, the microscopic $\text{Re}[\epsilon]$ (cyan dotted line) does not cross zero in the adjacent energy region. We only find that the macroscopic $\text{Re}[\epsilon]$ crosses the zero line, thus confirming the collective nature of the πP mode at small momentum transfers.

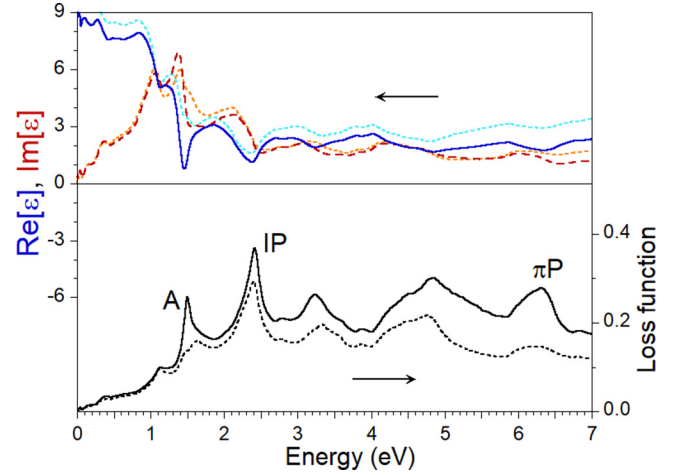


FIG. 10. Upper panel: Real (blue solid line) and imaginary (red dashed line) parts of the dielectric function in SrC₆ evaluated with the inclusion of the LFEs at momentum transfer $Q_{\parallel c^*} = 0.61 \text{ \AA}^{-1}$. The same quantities obtained without LFEs are shown by cyan and orange dotted lines, respectively. Lower panel: Loss function obtained with (black solid line) and without (black dotted line) inclusion of the LFEs. The peaks πP , IP, and A in the loss function are discussed in the text.

Along the c^* direction, the πP peak exhibits a positive parabolic-like dispersion from $\omega_{\pi P} \sim 5.2 \text{ eV}$ at small $Q_{\parallel c^*}$'s to $\omega_{\pi P} \sim 5.45 \text{ eV}$ at $Q_{\parallel c^*} = 0.13 \text{ \AA}^{-1}$. Thus, in SrC₆ the πP plasmon is a three-dimensional collective electronic excitation. Nevertheless, while in the carbon basal plane the πP peak possesses rather strong spectral weight, it is significantly weaker along the c^* direction. Its decay rate into the electron-hole pairs increases quickly upon increasing momentum transfer.

As can be seen in Figs. 6(g) and 9, at momentum transfers along the c^* direction the IP peak is located at significantly lower energies in comparison to that in the basal plane. At vanishing $Q_{\parallel c^*}$ its energy is 2.05 eV . Along the c^* axis the IP peak exhibits initial negative dispersion over the small momentum transfers range. Upon subsequent momentum increase it turns out to be positive and can be detected up to $\omega \sim 3 \text{ eV}$ at $Q_{\parallel c^*} \approx 1.1 \text{ \AA}^{-1}$. Again, such dispersion of the IP peak can be explained by the shape of the energy gap in $\text{Im}[\epsilon]$ of Fig. 6(i) between the intraband transition region IB3 and the interband one T with a lower border at 2.4 eV at small Q_{c^*} 's. With increasing momentum transfer the size of this gap gradually reduces and the IP peak width increases significantly in concert. Nevertheless, the IP peak in the loss function cannot be considered as the signature of a well-defined collective excitation in the whole momentum transfer range where it is observed. For instance, the dielectric and loss functions reported in Fig. 10 demonstrate that at $Q_{\parallel c^*} = 0.61 \text{ \AA}^{-1}$ the $\text{Re}[\epsilon]$ part does not cross zero in the energy interval where the IP peak is present in the loss function. Even though the LFEs bring the $\text{Re}[\epsilon]$ curve closer to zero, it is not sufficient to interpret the IP peak as a collective excitation at this $Q_{\parallel c^*}$. The same holds for the πP peak in the loss function. From Fig. 10 it is clear that at this momentum transfer the πP excitation loses its collective nature.

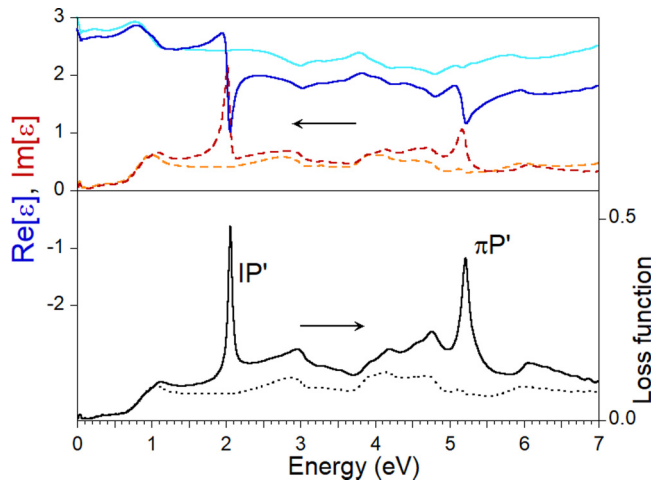


FIG. 11. Upper panel: Real (blue solid line) and imaginary (red dashed line) parts of the dielectric function in SrC₆ evaluated with the inclusion of the LFEs at momentum transfer $Q_{\parallel c^*} = 1.25 \text{ \AA}^{-1}$. The same quantities obtained without LFEs are shown by cyan and orange dotted lines, respectively. Lower panel: Loss function obtained with (black solid line) and without (black dotted line) inclusion of the LFEs. The peaks $\pi P'$ and IP' in the loss function are discussed in the text.

Additionally, in Fig. 6(g) one can observe in the loss function obtained with LFEs a rather sharp peak *A* at energies below 1.5 eV. Analyzing in Fig. 10 the behavior of the macroscopic $\text{Re}[\epsilon]$ (which reaches the value of 1 at $\omega = 1.45$ eV) and $\text{Im}[\epsilon]$ (which has a local minimum in the nearby energy interval with a sharp increase on the low-energy side) in the same figure we conclude that the *A* feature is not a true collective excitation. From Fig. 6(g) we determine that the *A* peak dispersion has a maximum at $Q_{\parallel c^*} = \pi/d$ and can be detected in the momentum transfer interval between 0.3 and 1.0 \AA^{-1} .

At momentum transfers along the c^* direction, the LFEs produce the appreciable transmittance of the spectral weight from the πP and IP peaks to the large momentum transfers. In particular, in Fig. 6(g) one can find additional peaks $\pi P'$ and IP' at $Q_{\parallel c^*}$'s in the vicinity of $Q_{\parallel c^*} = 2\pi/d$. Thus the LFEs are behind the reappearance at momentum transfers in the higher BZ's of both the πP and the IP modes along the direction perpendicular to the basal plane. This phenomenon was explained in detail for MgB₂ [80,81], graphite [88], and compressed lithium [82]. Note that the complete disappearance and the subsequent reappearance of the IP mode with increasing momentum transfer resembles the case of compressed lithium [82] and not that in MgB₂ and LiC₆ where continuous peak dispersion over subsequent BZ's is observed. To understand the nature of the $\pi P'$ and IP' peaks, in Fig. 11 we show the real and imaginary parts of the dielectric function and the loss function calculated at $Q_{\parallel c^*} = 1.25 \text{ \AA}^{-1}$. One can see that in the presented energy range the loss function obtained without LFEs is rather featureless and follows essentially the $\text{Im}[\epsilon]$ behavior. On the contrary, when the LFEs are taken into account, the loss function demonstrates two prominent peaks—the $\pi P'$ peak at an energy of 5.25 eV and the IP' peak at an energy of 2.05 eV. However, an analysis of

the macroscopic $\text{Re}[\epsilon]$ reported in the upper panel of Fig. 11 demonstrates that it does not reach zero at any energy. On the basis of this, both the $\pi P'$ and the IP' peaks in the loss function in SrC₆ along the c^* direction are difficult to classify as well-defined collective excitations.

An inspection of the low-energy excitation spectra in Fig. 6(g) reveals that the loss function along the c^* direction is rather different in comparison with that in the a^*-b^* plane. At small momentum transfers along the c^* axis, a peak with a soundlike dispersion does not appear in the calculated loss function. This correlates with a presence at the low energies of a single intraband $IB1$ peak in the $\text{Im}[\epsilon]$ reported in Fig. 6(i). This can be understood considering the DOS distribution in Fig. 8(c) where at the Fermi level only one nontrivial peak at $v_{\parallel c^*} = 0.13$ a.u. can be observed. However, in $\text{Im}[\epsilon]$ of Fig. 6(i) we can resolve at least two peaks $IB2$ and $IB3$ at ω 's exceeding 0.5 eV. The presence of these separate peaks in $\text{Im}[\epsilon]$ generates a peak *A* in the loss function discussed above.

3. BaC₆

The loss function of BaC₆ evaluated with the inclusion of the LFEs is shown in Figs. 12(a), 12(d), and 12(g). As in the previously discussed materials, these panels represent $L(\mathbf{Q}, \omega)$ at \mathbf{Q} 's along the a^* , b^* , and c^* symmetry directions, respectively. In the in-plane excitation spectra of Figs. 12(a) and 12(d), a most prominent feature is the πP plasmon corresponding to the collective response of the electrons mainly in the carbon π and π^* states. The energy of the πP peak at $Q_{\parallel a^*, b^*} = 0$ is 6.15 eV. Its dispersion is positive, and this mode can be observed up to energies above 12 eV at momentum transfers exceeding $\sim 1.2 \text{ \AA}^{-1}$. In general, the energy position and dispersion of the πP mode are similar to that in LiC₆, CaC₆, and SrC₆. However, one can find that in BaC₆ the amplitude of this mode is significantly reduced in comparison with other materials. This can be explained by the large amplitude of $\text{Im}[\epsilon]$ shown in Figs. 12(c) and 12(f) in the vicinity of the *T* peak located at an energy of 5.35 eV at $Q_{\parallel a^*, b^*} = 0$. Some details can be found in $\text{Im}[\epsilon]$ presented at small $Q_{\parallel b^*}$ in Fig. 13. The $\text{Im}[\epsilon]$ amplitude at energies around the *T* peak is larger in BaC₆ than in other systems. In the same figure, one can note that the real part of the dielectric function crosses the zero line at 5.8 eV, thus signaling about the collective nature of the πP mode. Nevertheless, the slope of the $\text{Re}[\epsilon]$ dispersion upon crossing the zero line is rather low due to the weakness of the *T* peak in $\text{Im}[\epsilon]$. This fact, in combination with elevated $\text{Im}[\epsilon]$ in the nearby energy region, results in the relatively low spectral weight of the πP peak in the loss function presenting a rather strong featureless background in Fig. 13. Indeed, in BaC₆, the πP plasmon efficiently decays into the electron-hole pairs. Moreover, the πP peak dispersion is strongly affected by interaction with the interband transitions. This is reflected in the formation of several separate peaks divided by the lower-intensity valleys along the πP dispersing branch, as seen in Figs. 12(a) and 12(d). Comparing these figures, one can detect some anisotropy in the in-plane πP peak dispersion. For instance, at finite momentum transfers its intensity varies considerably.

In the loss function of Fig. 13 on the upper-energy side of the πP peak we observe a broad peak with an energy of

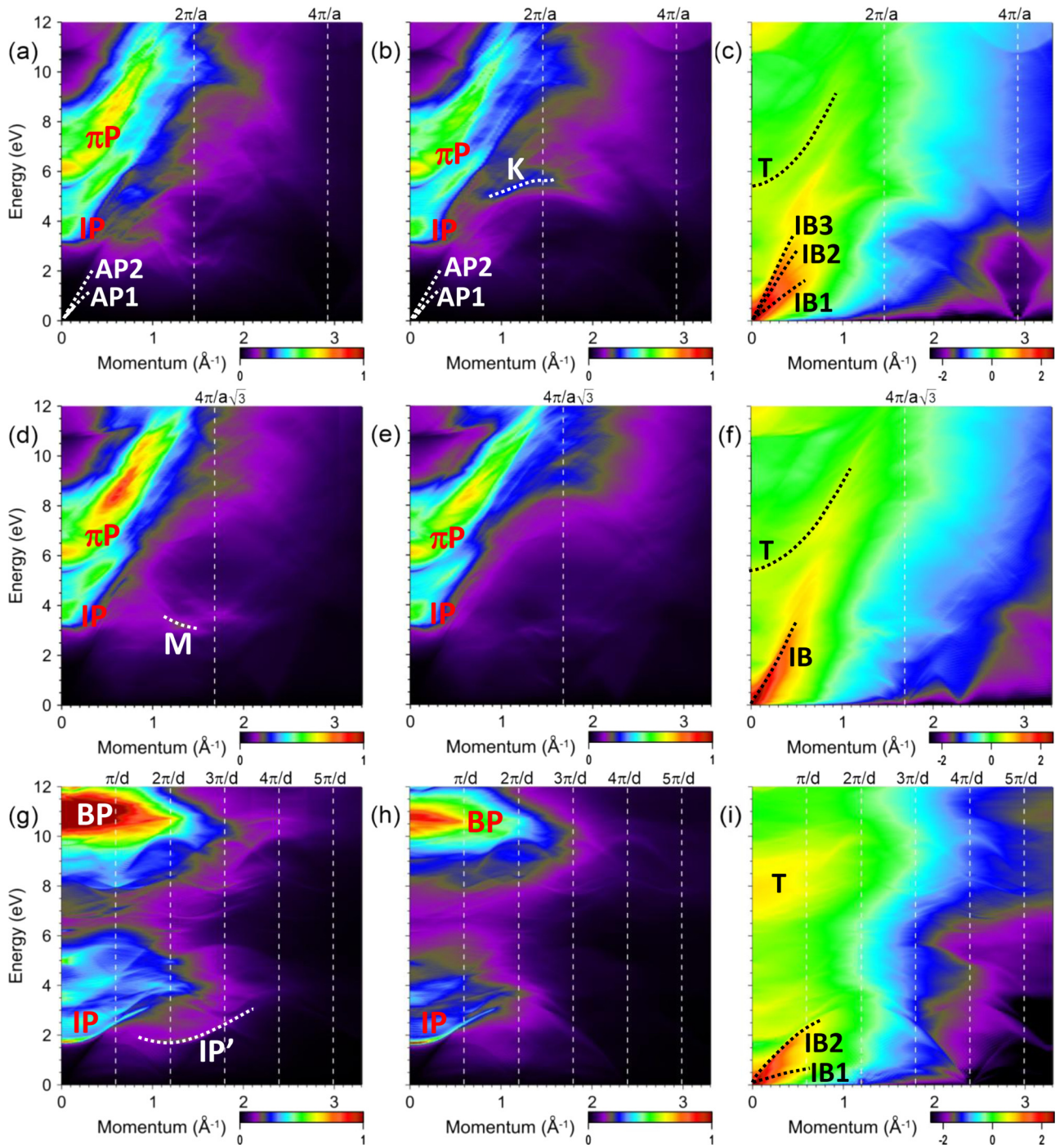


FIG. 12. Loss function, $L(\mathbf{Q}, \omega)$, of BaC_6 at momentum transfers \mathbf{Q} along the a^* axis calculated (a) with and (b) without inclusion of the local-field effects. The respective $\log_{10}\{\text{Im}[\epsilon]\}$ is shown in (c). In (d), (e), and (f) and in (g), (h), and (i) the same quantities are presented for \mathbf{Q} 's directed along the b^* and c^* axes, respectively. Peaks in the loss function corresponding to the bulk, π , intraband, and acoustic plasmons are labeled by BP, π P, IP, and AP, respectively. The peaks K, M, and IP' are discussed in the main text. The dispersion of the acoustic plasmon peaks AP1 and AP2 is highlighted by white dotted lines. In (c), (f), and (i) the peaks in $\text{Im}[\epsilon]$ generated by the intraband transitions are labeled by IB, IB1, IB2, and IB3, whose dispersion as well as that of the interband T peak is highlighted by black dotted lines.

7.65 eV. Its presence in the loss function can be linked to the interband peak in $\text{Im}[\epsilon]$ centered at an energy of ~ 7.1 eV. However, the strength of this peak in $\text{Im}[\epsilon]$ is not sufficient to make the $\text{Re}[\epsilon]$ curve approach the zero line in a nearby energy region. Based on such behavior of ϵ , we interpret this peak in the loss function as interband transitions. The

dispersion of this peak in Figs. 12(a) and 12(d) is positive and can be followed up to $Q \sim 0.2 \text{ \AA}^{-1}$, where it merges into the broad π P peak.

In the in-plane loss function of Figs. 12(a) and 12(d) at energies below the π P peak position, the other feature marked as IP can be detected. It possesses a positive dispersion in

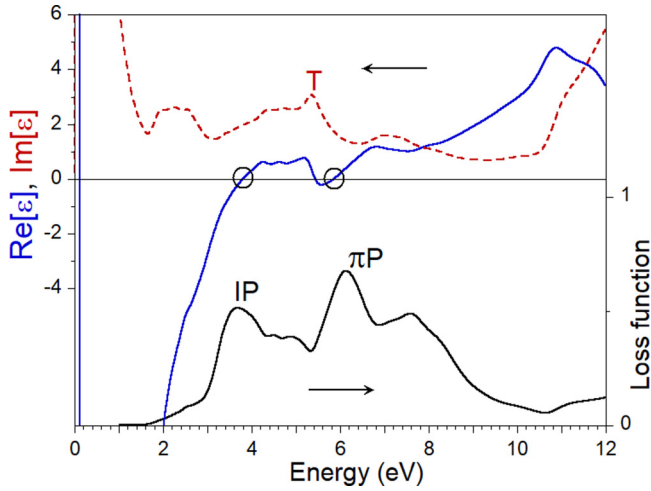


FIG. 13. Upper panel: Real (blue solid line) and imaginary (red dashed line) parts of the dielectric function in BaC_6 evaluated at momentum transfer $Q_{\parallel b^*} = 0.02 \text{ \AA}^{-1}$. Lower panel: The loss function obtained at the same $Q_{\parallel b^*}$ is shown by a black solid line. The interband peak T in $\text{Im}[\epsilon]$ produces a sharp drop in $\text{Re}[\epsilon]$ at the adjacent energy region via the Kramers-Kronig relation. The zero-crossings in $\text{Re}[\epsilon]$ producing the plasmon peaks IP and πP in the loss function are highlighted by open circles.

both in-plane symmetry directions and can be traced up to an energy of $\sim 7 \text{ eV}$ at $Q_{\parallel a^*} \sim 0.8 \text{ \AA}^{-1}$. Along the b^* direction, its dispersion can be detected up to $Q_{\parallel b^*} \sim 0.7 \text{ \AA}^{-1}$ where it reaches $\omega \sim 6.5 \text{ eV}$. At vanishing momentum transfers it has an energy of 3.7 eV . At small Q_{b^*} its properties can be seen in Fig. 13. Since $\text{Re}[\epsilon]$ crosses the zero line at almost the same energy, we interpret the IP peak in BaC_6 as a collective excitation.

A comparison of the loss function of Figs. 12(b) and 12(e) calculated without inclusion of the LFEs with that in Figs. 12(a) and 12(d) confirms some impact of the LFEs on the excitation spectra in BaC_6 . In Fig. 12(b) one can resolve a peak K with dispersion highlighted by the white dotted line. A detailed analysis of the dielectric function and the loss function allows us to conclude that this peak cannot be classified as a collective excitation. Moreover, upon inclusion of the LFEs, its presence in the loss function of Fig. 12(a) is almost completely suppressed. On the contrary, along the b^* axis we observe an opposite trend. A clear M peak in the loss function with the LFEs included, Fig. 12(d), has negligible intensity in the case of Fig. 12(e). We analyzed the M peak properties, and on the basis of the dielectric function behavior we concluded that it is not a collective excitation.

Another consequence of the inclusion of the LFEs is the notable variation in the intensity of the πP plasmon peak. In Figs. 12(a) and 12(d) one can see that the intensity of the πP peak is enhanced significantly upon the inclusion of the LFEs. This helps to extend the πP dispersion to larger momentum transfers and energies as well. The same, though at a smaller scale, is observed in the case of the IP peak.

At low energies and small momentum transfers in Figs. 12(a) and 12(b), we highlight with white dotted lines the dispersion of two peaks AP1 and AP2 with a soundlike

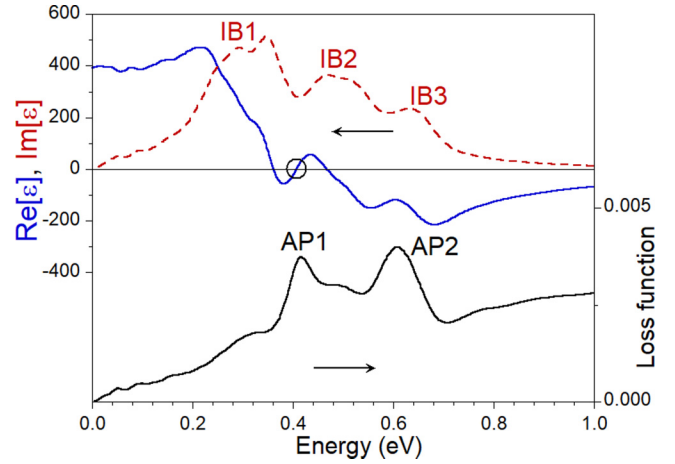


FIG. 14. Upper panel: Real (blue solid line) and imaginary (red dashed line) parts of the dielectric function in BaC_6 evaluated at momentum transfer $Q_{\parallel a^*} = 0.09 \text{ \AA}^{-1}$. The intraband peaks in $\text{Im}[\epsilon]$ generated by the states at the Fermi level moving with different group velocities are labeled as IB1 , IB2 , and IB3 . The zero-crossing of $\text{Re}[\epsilon]$ producing a peak AP1 in the loss function is highlighted by an open circle. Lower panel: Loss function (black solid line). Peaks in the loss function labeled as AP1 and AP2 correspond to the acoustic plasmons.

dispersion. Its existence is linked to the peculiar shape of the $\text{Im}[\epsilon]$ in this phase space related to the presence of several kinds of energy bands at the Fermi level. To understand the details, in Fig. 14 we present, as an example, the dielectric function and the loss function obtained at $Q_{\parallel a^*} = 0.09 \text{ \AA}^{-1}$. Two peaks IB1 and IB3 in $\text{Im}[\epsilon]$ are generated mainly by the intraband transitions within the energy bands at the Fermi level. In Fig. 15(a), with the DOS for the states moving in the a^* symmetry direction, we can discern at the Fermi level the peaks marked P1 and P3 . On the basis of the group velocities of these peaks at 0.23 and 0.48 a.u. , one can explain the peaks IB1 and IB3 in $\text{Im}[\epsilon]$ of Fig. 14. The origin of the IB2 peak remains unclear. It is probably linked to the peak P2 in the DOS of Fig. 15(a) centered at $v_{\parallel a^*} = 0.37 \text{ a.u.}$ in close proximity to E_F . The presence of the peaks IB1 and IB2 in $\text{Im}[\epsilon]$ of Fig. 14 causes the real part of the dielectric function to cross the zero line at $\omega = 0.41 \text{ eV}$. In combination with a local minimum in $\text{Im}[\epsilon]$ in the adjacent energy interval, it signals the collective nature of the AP1 mode.

The situation with the AP2 peak in the loss function is more involved. The spectral weight of this peak is considerably larger than that of the AP1 mode. On the other hand, the real part of the dielectric function does not cross the zero line in the energy interval close to the AP2 energy. Indeed, at that energy the $\text{Re}[\epsilon]$ part exceeds a value of -100 . Nevertheless, based on the spectral weight in the loss function (which is a quantity directly probed in the experiment), we classify it as a plasmonic excitation as well. Since the energy positions of the peaks IB1 , IB2 , and IB3 in $\text{Im}[\epsilon]$ of Fig. 12(c) change fairly linearly upon an increase in momentum transfer magnitude, the dispersion of the AP1 and AP2 peaks presents a soundlike dispersion as well. In Fig. 12(a) the dispersion of the AP1 peak can be detected up to an energy of about 1 eV . In

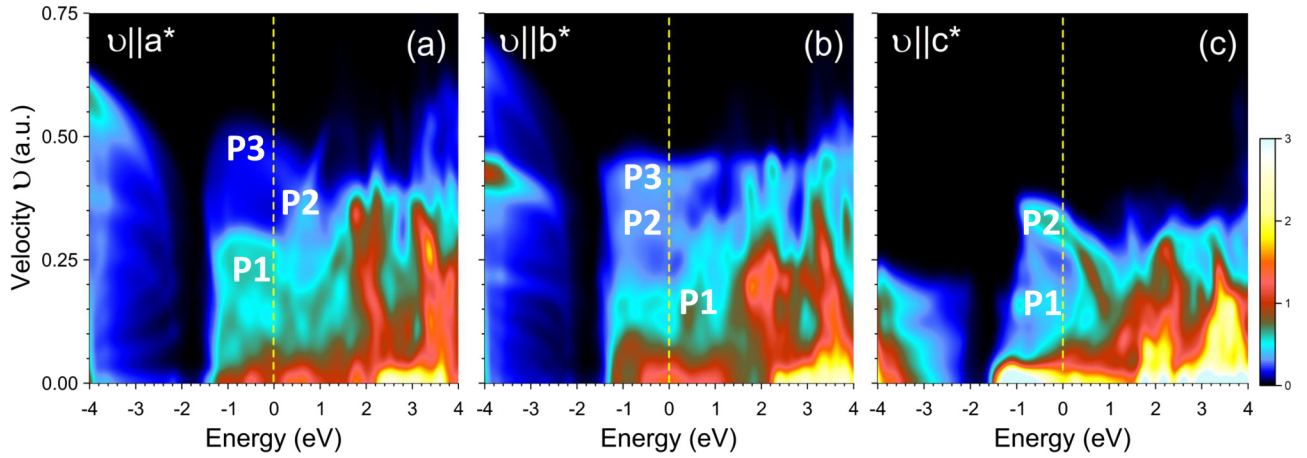


FIG. 15. Density of states distribution in BaC_6 vs energy and group velocity components along (a) a^* , (b) b^* , and (c) c^* symmetry directions. Peaks at the Fermi level are labeled as P1, P2, and P3. The energies are relative to the Fermi level set to zero.

the case of the AP2 peak, its energy reaches $\omega \approx 2.1$ eV. Note that the LFEs play a marginal role in the formation of both mode properties. The realization of more than one acoustic mode was found previously in Pd [58,76] and Pb [89]. The peculiarity of the AP1 and AP2 excitations in BaC_6 is its existence in the a^* symmetry direction only. In the loss function of Fig. 12(d) for momentum transfers along the b^* axis we do not find similar peaks despite the fact that at least three P1, P2, and P3 peaks [see Fig. 15(b)] reside at the Fermi level in the DOS of the states moving in that direction.

The loss function in BaC_6 at momentum transfers along the c^* symmetry direction obtained with and without the LFEs is reported, respectively, in Figs. 12(g) and 12(h). One can see that excitation spectrum in the direction perpendicular to the basal plane differs substantially from the in-plane one. A most notable difference is the presence in the loss function, Fig. 12(g), of the BP peak corresponding to the bulk plasmon. At $Q_{\parallel c^*} = 0$ its energy is 10.85 eV. The width of the BP peak is about 1 eV. We explain its reduced energy along the c^* axis by the presence of an intense broad peak centered at $\omega \approx 8$ eV in $\text{Im}[\epsilon]$ in Fig. 12(i). In the particular case of $Q_{\parallel c^*} = 0.02 \text{ \AA}^{-1}$ of Fig. 16, its presence in $\text{Im}[\epsilon]$ forces the real part of the dielectric function to cross the zero line at slightly larger energy. Upon an energy increase, $\text{Re}[\epsilon]$ crosses the zero line again with a positive slope at $\omega \approx 10.6$ eV, where $\text{Im}[\epsilon]$ is small, i.e., the conditions for the existence of well-defined collective excitations are fulfilled. From a comparison of Figs. 12(g) and 12(h), one can deduce that the LFEs strongly enhance the intensity of the BP peak in the loss function and expand the momentum transfer range where this mode can be detected. In more details, the properties of the BP plasmon can be seen in Fig. 16, where one can appreciate at which scale the LFEs influence the BP mode characteristics at $Q_{\parallel c^*} = 0.02 \text{ \AA}^{-1}$. For instance, the BP energy increases by 0.1 eV due to the LFEs. Moreover, the BP peak amplitude is enhanced considerably while its width is reduced. In Fig. 12(g) the BP peak dispersion is initially almost flat and becomes negative at larger momentum transfers. It can be detected up to about $Q_{\parallel c^*} = 2 \text{ \AA}^{-1}$, where its energy is reduced to 10.2 eV.

In the loss function in Fig. 12(g) we can observe a sharp IP peak with an energy of 1.7 eV at vanishing momentum transfer. As in the other two systems under study, we interpret it as an intraband plasmon peak. The dispersion of the IP peak is positive and can be traced up to an energy of about 3 eV. In Fig. 16 one can see that the LFE's modify the IP properties, shifting their energy upward by about 0.05 eV and reducing their intensity. Almost the same energy shift of the IP peak due to the LFEs holds over its entire dispersion. In Fig. 16 one can clearly see that the LFEs strongly enhance the loss function amplitude at energies above ω_{IP} . This also occurs at final momentum transfers, as can be deduced from a comparison of Figs. 12(g) and 12(h). In particular, several peaks in the loss function of Fig. 12(g) can be detected in the

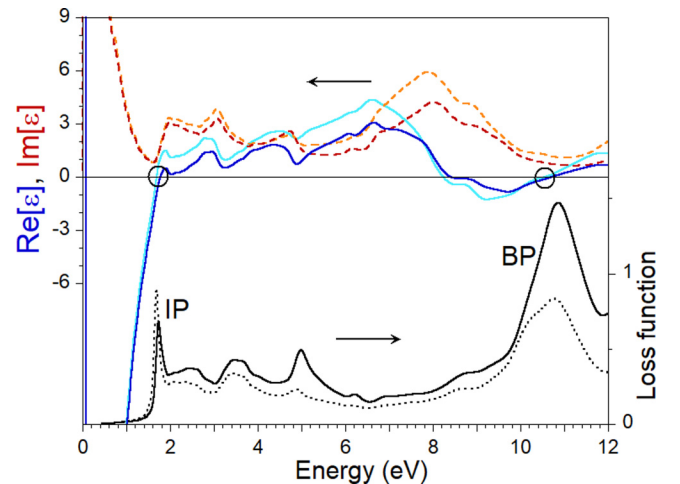


FIG. 16. Upper panel: Real (blue solid line) and imaginary (red dashed line) parts of the dielectric function in BaC_6 evaluated with the inclusion of the LFE's at momentum transfer $Q_{\parallel c^*} = 0.02 \text{ \AA}^{-1}$. The same quantities obtained without the LFE's are shown by cyan and orange dotted lines, respectively. Lower panel: Loss function with (black solid line) and without (black dotted line) inclusion of the LFE's. The zero-crossings in $\text{Re}[\epsilon]$ producing the IP and BP peaks in the loss function are highlighted by open circles.

2–7 eV interval. An analysis of the real part of the dielectric function in Fig. 16 in this energy interval reveals that the LFEs shift it downward strongly to the zero line. Nevertheless, since in the referred energy interval $\text{Re}[\epsilon]$ does not cross the zero line, we do not classify the other peaks in the loss function apart from the IP and BP ones as collective excitations. Hence the π P plasmon is not realized in the c^* symmetry direction. Thus in BaC_6 it is a two-dimensional excitation, as occurs in LiC_6 .

One of the consequences of the LFEs inclusion is the appearance of the IP' peak at finite momentum transfers in the loss function given in Fig. 12(g). Its dispersion, marked by a white dotted line, has a parabolic-like shape with a minimum at $Q_{\parallel c^*} = 2\pi/d$. Its dispersion can be detected up to an energy of about 3 eV. From an analysis of the dielectric function behavior, we conclude that it is not collective excitation.

Finally, in the low-energy interval we do not find in the loss function of Fig. 12(g) [also in Fig. 12(h)] any signature of peaks with characteristic soundlike dispersion. Even though in the $\text{Im}[\epsilon]$ presented in Fig. 12(i) we find two clear IB1 and IB2 peaks [originated from the P1 and P2 peaks in the DOS of Fig. 15(c)] whose energies increase linearly upon energy increase, such a mode in the loss function does not appear. This confirms that the mere fact of the presence of a two-peak structure in $\text{Im}[\epsilon]$ does not guarantee the existence of an acoustic plasmon.

IV. CONCLUSIONS

In this theoretical study, we have reported the results of the *ab initio* calculations of the dynamical momentum-dependent dielectric properties of LiC_6 , SrC_6 , and BaC_6 in the 0–12 eV energy range. Calculations were performed within the RPA framework with the full inclusion of the local-field effects. Our results demonstrate that doping graphite with different atoms strongly modifies its electronic and, subsequently, dielectric properties in this energy region.

In particular, the intercalation with Sr and Ba produces the strong downward shift of the bulk plasmon (BP) at the momentum transfers in the direction perpendicular to the carbon basal plane. The BP peak dominates the excitation spectra of SrC_6 and BaC_6 in the investigated energy interval with an energy of 11.1 and 10.85 eV, respectively, at $Q_{\parallel c^*} = 0$. The dispersion of this mode with momentum transfer increase is negative. In LiC_6 , the BP is located at a higher energy.

Regarding the π plasmon (π P), in all the studied systems its properties vary substantially. In LiC_6 and BaC_6 , it is realized at the in-plane momentum transfers, i.e., is a 2D quantity. At vanishing momentum transfers its energy is 6.2 eV in LiC_6 and 6.15 eV in BaC_6 . On the contrary, in SrC_6 the π plasmon can be found in all three symmetry directions, thus being 3D excitations. However, its energy is different at the in-plane and out-of-plane momentum transfers. At vanishing $Q_{\parallel a^*}$ and $Q_{\parallel b^*}$ its energy is 6.4 eV, whereas at small $Q_{\parallel c^*}$ it is 5.2 eV. The dispersion of this mode in SrC_6 is positive.

The doping of graphite with the intercalant electrons gives rise to the intraband plasmon (IP) frequently observed in the layered systems [39,90–93]. In LiC_6 , SrC_6 , and BaC_6 it is

found in all symmetry directions. However, the considered systems present a large variety regarding the IP properties. At small in-plane momentum transfers, its energy is 2.6, 3.65, and 3.7 eV in LiC_6 , SrC_6 , and BaC_6 , respectively. As for the in-plane IP dispersion, it is positive in LiC_6 , negative in SrC_6 , and positive in BaC_6 . At $Q_{\parallel c^*} = 0$, the energy of the IP mode is 1.7, 2.05, and 1.7 eV. The peculiarity of this mode in LiC_6 is that its dispersion is almost flat over an extended momentum transfer range governed by the local-field effects. As for SrC_6 and BaC_6 , the IP peak has negative and positive dispersion, respectively.

The substantial modifications in the electronic structure at the Fermi level upon intercalation produce a strong variation in the low-energy dielectric properties of these compounds. Special impact is introduced by the filling of the interlayer energy band of graphite, which becomes partly occupied in SrC_6 and BaC_6 , staying totally unoccupied in LiC_6 . Such variation most notably is manifested in the appearance of an acoustic plasmon with characteristic soundlike dispersion in certain cases. Thus it is absent in LiC_6 , which we attribute to the presence at the Fermi level of only the π^* carbon-derived energy bands. On the contrary, in SrC_6 and BaC_6 , where the interlayer band crosses the Fermi level, the acoustic plasmon is detected in certain momentum transfer directions. Thus in SrC_6 such a mode is found at energies below 1 eV at the in-plane momentum transfers. In the case of BaC_6 , the situation is rather peculiar. At momentum transfers along the a^* symmetry direction, we found two plasmons with soundlike dispersion. One can be observed up to an energy of about 1 eV, whereas the second mode disperses up to an energy of about 2 eV. On the contrary, at momentum transfers along the b^* symmetry direction we do not find any signature of such a mode, and we find that the same is true along the c^* direction.

Additionally, in these materials we found several sometimes prominent peaks in the calculated loss function. However, an analysis of the dielectric function in the nearby energy region allowed us to interpret them as single-particle excitations.

A comparison of the excitation spectra obtained with and without inclusion of the local-field effects demonstrates that in these three compounds the LFEs have a strong impact on the dielectric properties. At finite momentum transfers, the LFEs notably redistribute the spectral weight between different regions in the momentum-energy space. In this respect, it is difficult to make a general conclusion. In some cases the LFEs enhance the spectral weight of certain features in the loss function, while in other cases they suppress them. The most striking manifestation of the LFEs was observed in LiC_6 , where they flatten the IP plasmon dispersion over an extended momentum transfer range.

ACKNOWLEDGMENTS

E.V.C. and V.M.S. acknowledge the partial support from the University of the Basque Country UPV/EHU, Grant No. IT-756-13 and the Spanish Ministry of Economy, Industry and Competitiveness MINEICO, Projects No. FIS2016-76617-P and No. FIS2016-75862-P. V.M.S. acknowledges the project PI2017-30 of the Departamento de Educación, Política Lingüística y Cultura of the Basque government.

- [1] M. S. Dresselhaus and G. Dresselhaus, *Adv. Phys.* **30**, 139 (1981).
- [2] T. Enoki, M. Suzuki, and M. Endo, *Graphite Intercalated Compounds and Applications* (Oxford University Press, Oxford, 2003).
- [3] T. E. Weller, M. Ellerby, S. S. Saxena, R. P. Smith, and N. T. Skipper, *Nat. Phys.* **1**, 39 (2005).
- [4] R. P. Smith, T. E. Weller, C. A. Howard, M. P. M. Dean, K. C. Rahnejat, S. S. Saxena, and M. Ellerby, *Physica C* **514**, 50 (2015).
- [5] J. S. Kim, L. Boeri, J. R. O'Brien, F. S. Razavi, and R. K. Kremer, *Phys. Rev. Lett.* **99**, 027001 (2007).
- [6] S. Heguri, N. Kawade, T. Fujisawa, A. Yamaguchi, A. Sumiyama, K. Tanigaki, and M. Kobayashi, *Phys. Rev. Lett.* **114**, 247201 (2015).
- [7] M. Calandra, C. Attacalite, G. Profeta, and F. Mauri, *Phys. Rev. Lett.* **108**, 149701 (2012).
- [8] G. Profeta, M. Calandra, and F. Mauri, *Nat. Phys.* **8**, 131 (2012).
- [9] C. Kramberger, F. Roth, R. Schuster, R. Kraus, M. Knupfer, E. Einarsson, S. Maruyama, D. J. Mowbray, A. Rubio, and T. Pichler, *Phys. Rev. B* **85**, 085424 (2012).
- [10] Z.-H. Pan, J. Camacho, M. H. Upton, A. V. Fedorov, C. A. Howard, M. Ellerby, and T. Valla, *Phys. Rev. Lett.* **106**, 187002 (2011).
- [11] N. Emery, C. Hérold, M. d'Astuto, V. Garcia, C. Bellin, J. F. Maréché, P. Lagrange, and G. Loupías, *Phys. Rev. Lett.* **95**, 087003 (2005).
- [12] A. Grüneis, C. Attacalite, A. Rubio, D. V. Vyalikh, S. L. Molodtsov, J. Fink, R. Follath, W. Eberhardt, B. Büchner, and T. Pichler, *Phys. Rev. B* **79**, 205106 (2009).
- [13] M. H. Upton, A. C. Walters, C. A. Howard, K. C. Rahnejat, M. Ellerby, J. P. Hill, D. F. McMorrow, A. Alatas, B. M. Leu, and W. Ku, *Phys. Rev. B* **76**, 220501(R) (2007).
- [14] J. C. Chacón-Torres, L. Wirtz, and T. Pichler, *Phys. Status Solidi B* **251**, 2337 (2014).
- [15] T. Bazhiron, Y. Sakai, S. Saito, and M. L. Cohen, *Phys. Rev. B* **89**, 045136 (2014).
- [16] S. Nakamae, A. Gauzzi, F. Ladieu, D. L'Hôte, N. Eméry, C. Hérold, J. F. Maréché, P. Lagrange, and G. Loupías, *Solid State Commun.* **145**, 493 (2008).
- [17] M. Calandra and F. Mauri, *Phys. Status Solidi B* **243**, 3458 (2006).
- [18] Y. Takada, *J. Supercond. Nov. Mag.* **22**, 89 (2009).
- [19] D. G. Hinks, D. Rosenmann, H. Claus, M. S. Bailey, and J. D. Jorgensen, *Phys. Rev. B* **75**, 014509 (2007).
- [20] M. P. M. Dean, A. C. Walters, C. A. Howard, T. E. Weller, M. Calandra, F. Mauri, M. Ellerby, S. S. Saxena, A. Ivanov, and D. F. McMorrow, *Phys. Rev. B* **82**, 014533 (2010).
- [21] A. Sanna, G. Profeta, A. Floris, A. Marini, E. K. U. Gross, and S. Massidda, *Phys. Rev. B* **75**, 020511(R) (2007).
- [22] J. S. Kim, R. K. Kremer, L. Boeri, and F. S. Razavi, *Phys. Rev. Lett.* **96**, 217002 (2006).
- [23] I. I. Mazin, L. Boeri, O. V. Dolgov, A. A. Golubov, G. B. Bachelet, M. Giantomassi, and O. K. Andersen, *Physica C* **460**, 116 (2007).
- [24] I. I. Mazin, *Phys. Rev. Lett.* **95**, 227001 (2005).
- [25] A. C. Walters, C. A. Howard, M. H. Upton, M. P. M. Dean, A. Alatas, B. M. Leu, M. Ellerby, D. F. McMorrow, J. P. Hill, M. Calandra, and F. Mauri, *Phys. Rev. B* **84**, 014511 (2011).
- [26] S.-L. Yang, J. A. Sobota, C. A. Howard, C. J. Pickard, M. Hashimoto, D. H. Lu, S.-K. Mo, P. S. Kirchmann, and Z.-X. Shen, *Nat. Commun.* **5**, 3493 (2014).
- [27] W. Kyung, Y. Kim, G. Han, C. Leem, C. Kim, Y. Koh, B. Kim, Y. Kim, J. S. Kim, K. S. Kim, E. Rotenberg, J. D. Denlinger, and C. Kim, *Phys. Rev. B* **92**, 224516 (2015).
- [28] N. A. W. Holzwarth, S. Rabi, and L. A. Girifalco, *Phys. Rev. B* **18**, 5190 (1978).
- [29] W. Eberhardt, I. T. McGovern, E. W. Plummer, and J. E. Fischer, *Phys. Rev. Lett.* **44**, 200 (1980).
- [30] D. P. DiVincenzo and S. Rabi, *Phys. Rev. B* **25**, 4110 (1982).
- [31] G. Csányi, P. B. Littlewood, A. H. Nevidomskyy, C. J. Pickard, and B. D. Simons, *Nat. Phys.* **1**, 42 (2005).
- [32] B. T. Geilikman, *Usp. Fiz. Nauk* **88**, 327 (1966) [*Sov. Phys. Usp.* **9**, 142 (1966)].
- [33] E. A. Pashitski, *Zh. Eksp. Teor. Fiz.* **55**, 2387 (1969) [*Sov. Phys. JETP* **28**, 1267 (1969)].
- [34] Y. A. Uspenskii, *Zh. Eksp. Teor. Fiz.* **76**, 1620 (1979) [*Sov. Phys. JETP* **49**, 822 (1979)].
- [35] H. Fröhlich, *J. Phys. C* **1**, 544 (1968).
- [36] B. M. Ludbrook, G. Levy, P. Nigge, M. Zonno, M. Schneider, D. J. Dvorak, C. N. Veenstra, S. Zhdanovich, D. Wong, P. Dosanjh, C. Straßer, A. Stöhr, S. Forti, C. R. Ast, U. Starke, and A. Damascelli, *Proc. Natl. Acad. Sci. (USA)* **112**, 11795 (2015).
- [37] S. Ichinokura, K. Sugawara, A. Takayama, T. Takahashi, and S. Hasegawa, *ACS Nano* **10**, 2761 (2016).
- [38] J. Chapman, Y. Su, C. A. Howard, D. Kundys, A. N. Grigorenko, F. Guinea, A. K. Geim, I. V. Grigorieva, and R. R. Nair, *Sci. Rep.* **6**, 23254 (2016).
- [39] J. P. Echeverry, E. V. Chulkov, P. M. Echenique, and V. M. Silkin, *Phys. Rev. B* **85**, 205135 (2012).
- [40] F. Roth, A. König, C. Kramberger, T. Pichler, B. Büchner, and M. Knupfer, *Europhys. Lett.* **102**, 17001 (2013).
- [41] V. M. Silkin, A. García-Lekue, J. M. Pitarke, E. V. Chulkov, E. Zaremba, and P. M. Echenique, *Europhys. Lett.* **66**, 260 (2004).
- [42] B. Diaconescu, K. Pohl, L. Vattuone, L. Savio, P. Hofmann, V. M. Silkin, J. M. Pitarke, E. V. Chulkov, P. M. Echenique, D. Fariás, and M. Rocca, *Nature (London)* **448**, 57 (2007).
- [43] S. J. Park and R. E. Palmer, *Phys. Rev. Lett.* **105**, 016801 (2010).
- [44] K. Pohl, B. Diaconescu, G. Vercelli, L. Vattuone, V. M. Silkin, E. V. Chulkov, P. M. Echenique, and M. Rocca, *Europhys. Lett.* **90**, 57006 (2010).
- [45] J. Pischel, E. Welsch, O. Skibbe, and A. Pucci, *J. Phys. Chem. C* **117**, 26964 (2013).
- [46] D. Guerard, M. Chabouni, P. Lagrange, M. F. Makrini, and A. Herold, *Carbon* **18**, 257 (1980).
- [47] V. M. Silkin, E. V. Chulkov, I. Y. Sklyadneva, and V. E. Panin, *Izv. Vyssh. Uchebn. Zaved. Fiz.* **9**, 56 (1984) [*Sov. Phys. J.* **27**, 762 (1984)].
- [48] N. Troullier and J. L. Martins, *Phys. Rev. B* **43**, 1993 (1991).
- [49] D. M. Ceperley and B. J. Alder, *Phys. Rev. Lett.* **45**, 566 (1980); as parametrized by J. P. Perdew and A. Zunger, *Phys. Rev. B* **23**, 5048 (1981).
- [50] E. Runge and E. K. U. Gross, *Phys. Rev. Lett.* **52**, 997 (1984).
- [51] M. Petersilka, U. J. Gossmann, and E. K. U. Gross, *Phys. Rev. Lett.* **76**, 1212 (1996).
- [52] E. K. U. Gross and W. Kohn, *Phys. Rev. Lett.* **55**, 2850 (1985).

- [53] A. G. Marinopoulos, L. Reining, V. Olevano, A. Rubio, T. Pichler, X. Liu, M. Knupfer, and J. Fink, *Phys. Rev. Lett.* **89**, 076402 (2002).
- [54] V. M. Silkin, E. V. Chulkov, and P. M. Echenique, *Phys. Rev. B* **68**, 205106 (2003).
- [55] F. Aryasetiawan and O. Gunnarsson, *Phys. Rev. B* **49**, 16214 (1994).
- [56] F. Aryasetiawan, in *Strong Coulomb Correlations in Electronic Structure Calculations*, edited by V. I. Anisimov (Gordon and Beach, Singapore, 2001).
- [57] V. P. Zhukov, F. Aryasetiawan, E. V. Chulkov, and P. M. Echenique, *Phys. Rev. B* **65**, 115116 (2002).
- [58] V. M. Silkin, I. P. Chernov, Yu. M. Koroteev, and E. V. Chulkov, *Phys. Rev. B* **80**, 245114 (2009).
- [59] S. L. Adler, *Phys. Rev.* **126**, 413 (1962).
- [60] N. Wiser, *Phys. Rev.* **129**, 62 (1963).
- [61] M. Calandra and F. Mauri, *Phys. Rev. B* **74**, 094507 (2006).
- [62] E. V. Chulkov, Y. M. Koroteev, and V. M. Silkin, *Surf. Sci.* **247**, 115 (1991).
- [63] L. A. Grunes, I. P. Gates, J. J. Ritsko, E. J. Mele, D. P. DiVincenzo, M. E. Preil, and J. E. Fischer, *Phys. Rev. B* **28**, 6681 (1983).
- [64] N.-X. Chen and S. Rabii, *Phys. Rev. Lett.* **52**, 2386 (1984).
- [65] J. J. Ritsko and M. J. Rice, *Phys. Rev. Lett.* **42**, 666 (1979).
- [66] E. A. Taft and H. R. Philipp, *Phys. Rev.* **138**, A197 (1965).
- [67] L. A. Grunes and J. J. Ritsko, *Phys. Rev. B* **28**, 3439 (1983).
- [68] D. M. Hwang, M. Utlaut, M. S. Isaacson, and S. A. Solin, *Phys. Rev. Lett.* **43**, 882 (1979).
- [69] J. J. Ritsko and E. J. Mele, *Phys. Rev. B* **21**, 730 (1980).
- [70] J. J. Ritsko, E. J. Mele, and I. P. Gates, *Phys. Rev. B* **24**, 6114 (1981).
- [71] M. E. Preil, L. A. Grunes, J. J. Ritsko, and J. E. Fischer, *Phys. Rev. B* **30**, 5852 (1984).
- [72] F. J. Nelson, J.-C. Idrobo, J. D. Fite, Z. L. Mišković, S. J. Pennycook, S. T. Pantelides, J. U. Lee, and A. C. Diebold, *Nano Lett.* **14**, 3827 (2014).
- [73] S. C. Liou, C.-S. Shie, C. H. Chen, R. Breitwieser, W. W. Pai, G. Y. Guo, and M.-W. Chu, *Phys. Rev. B* **91**, 045418 (2015).
- [74] D. Novko, V. Despoja, and M. Šunjić, *Phys. Rev. B* **91**, 195407 (2015).
- [75] D. Pines and P. Nozières, *The Theory of Quantum Liquids: Normal Fermi Liquids* (Benjamin, New York, 1966), Vol. 1.
- [76] V. M. Silkin, V. U. Nazarov, A. Balassis, I. P. Chernov, and E. V. Chulkov, *Phys. Rev. B* **94**, 165122 (2016).
- [77] J. E. Fischer, J. M. Bloch, C. C. Shieh, M. E. Preil, and K. Jelley, *Phys. Rev. B* **31**, 4773 (1985).
- [78] S. Basu, C. Zeller, P. J. Flanders, C. D. Fuerst, W. D. Johnson, and J. E. Fischer, *Mater. Sci. Eng.* **38**, 275 (1979).
- [79] N. Barrett, E. E. Krasovskii, J.-M. Themlin, and V. N. Strocov, *Phys. Rev. B* **71**, 035427 (2005).
- [80] Y. Q. Cai, P. C. Chow, O. D. Restrepo, Y. Takano, K. Togano, H. Kito, H. Ishii, C. C. Chen, K. S. Liang, C. T. Chen, S. Tsuda, S. Shin, C. C. Kao, W. Ku, and A. G. Eguiluz, *Phys. Rev. Lett.* **97**, 176402 (2006).
- [81] A. Balassis, E. V. Chulkov, P. M. Echenique, and V. M. Silkin, *Phys. Rev. B* **78**, 224502 (2008).
- [82] I. Errea, A. Rodriguez-Prieto, B. Rousseau, V. M. Silkin, and A. Bergara, *Phys. Rev. B* **81**, 205105 (2010).
- [83] V. M. Silkin, A. Balassis, P. M. Echenique, and E. V. Chulkov, *Phys. Rev. B* **80**, 054521 (2009).
- [84] P. Cudazzo and M. Gatti, *Phys. Rev. B* **96**, 125131 (2017).
- [85] L. Marušić and V. Despoja, *Phys. Rev. B* **95**, 201408(R) (2017).
- [86] I. V. Silkin, I. P. Chernov, V. M. Silkin, and E. V. Chulkov, *Phys. Rev. B* **98**, 075111 (2018).
- [87] D. Pines, *Elementary Excitations in Solids* (Benjamin, New York, 1963).
- [88] R. Hambach, C. Giorgetti, N. Hiraoka, Y. Q. Cai, F. Sottile, A. G. Marinopoulos, F. Bechstedt, and L. Reining, *Phys. Rev. Lett.* **101**, 266406 (2008).
- [89] X. Zubizarreta, V. M. Silkin, and E. V. Chulkov, *Phys. Rev. B* **87**, 115112 (2013).
- [90] V. P. Zhukov, V. M. Silkin, E. V. Chulkov, and P. M. Echenique, *Phys. Rev. B* **64**, 180507(R) (2001).
- [91] W. Ku, W. E. Pickett, R. T. Scalettar, and A. G. Eguiluz, *Phys. Rev. Lett.* **88**, 057001 (2002).
- [92] J. van Wezel, R. Schuster, A. König, M. Knupfer, J. van den Brink, H. Berger, and B. Büchner, *Phys. Rev. Lett.* **107**, 176404 (2011).
- [93] M. N. Faraggi, A. Arnau, and V. M. Silkin, *Phys. Rev. B* **86**, 035115 (2012).